WILEY

RESEARCH ARTICLE

A concise and persistent feature to study brain resting-state network dynamics: Findings from the Alzheimer's Disease Neuroimaging Initiative

Liqun Kuang[1,2] | Xie Han[1] | Kewei Chen[3] | Richard J. Caselli[4] | Eric M. Reiman[3] |
Yalin Wang[2] | for the Alzheimer's Disease Neuroimaging Initiative

[1]School of Computer Science and Technology, North University of China, Taiyuan, Shanxi, China

[2]School of Computing, Informatics, and Decision Systems Engineering, Arizona State University, Tempe, Arizona

[3]Banner Alzheimer's Institute, Phoenix, Arizona

[4]Department of Neurology, Mayo Clinic Arizona, Scottsdale, Arizona

Correspondence
Liqun Kuang, School of Computer Science and Technology, North University of China, Taiyuan, Shanxi, China.
Email: kuang@nuc.edu.cn
and
Yalin Wang, School of Computing, Informatics, and Decision Systems Engineering, Arizona State University, P.O. Box 878809, Tempe, AZ 85287.
Email: ylwang@asu.edu

Abstract

Alzheimer's disease (AD) is the most common type of dementia in the elderly with no effective treatment currently. Recent studies of noninvasive neuroimaging, resting-state functional magnetic resonance imaging (rs-fMRI) with graph theoretical analysis have shown that patients with AD and mild cognitive impairment (MCI) exhibit disrupted topological organization in large-scale brain networks. In previous work, it is a common practice to threshold such networks. However, it is not only difficult to make a principled choice of threshold values, but also worse is the discard of potential important information. To address this issue, we propose a threshold-free feature by integrating a prior persistent homology-based topological feature (the zeroth Betti number) and a newly defined connected component aggregation cost feature to model brain networks over all possible scales. We show that the induced topological feature (Integrated Persistent Feature) follows a monotonically decreasing convergence function and further propose to use its slope as a concise and persistent brain network topological measure. We apply this measure to study rs-fMRI data from the Alzheimer's Disease Neuroimaging Initiative and compare our approach with five other widely used graph measures across five parcellation schemes ranging from 90 to 1,024 region-of-interests. The experimental results demonstrate that the proposed network measure shows more statistical power and stronger robustness in group difference studies in that the absolute values of the proposed measure of AD are lower than MCI and much lower than normal controls, providing empirical evidence for decreased functional integration in AD dementia and MCI.

Abbreviations: AD, Alzheimer's disease; ADNI, Alzheimer's Disease Neuroimaging Initiative; ALFF, amplitude of low-frequency fluctuations; BNP, the zeroth Betti numbers plot; BOLD, blood oxygen level dependent; CDR, clinical dementia rating; CPL, characteristic path length; EC, eigenvector centrality; FC, functional connectivity; FDG, fludeoxyglucose; H-1024, randomly generated high-resolution atlas with 1,024 ROIs; ICA, independent component analysis; IPF, Integrated Persistent Feature; L-AAL116, low-resolution automated anatomical labeling atlas with 116 ROIs; L-AAL90, low-resolution automated anatomical labeling atlas with 90 ROIs; L-Crad200, low-resolution Craddock et al. functional atlas with 200 ROIs; L-HOA112, low-resolution Harvard-Oxford atlas with 112 ROIs; MCI, mild cognitive impairment; MMSE, Mini-Mental Status Examination; Mod, modularity; MRI, magnetic resonance imaging; MST, minimum spanning tree; NC, normal control; ND, network diameter; PET, positron emission tomography; ReHo, regional homogeneity; ROI, region-of-interest; rs-fMRI, resting-state functional magnetic resonance imaging; RSN, resting-state network; SIP, slope of IPF plot; SLD, single linkage dendrogram; SLFF, spontaneous low-frequency fluctuations

1 | INTRODUCTION

Alzheimer's disease (AD) is a progressive neurodegenerative disorder which is mainly characterized by significant impairments in a global cognitive decline (Bernhardt, Chen, He, Evans, & Bernasconi, 2011; DeSalvo, Douw, Tanaka, Reinsberger, & Stufflebeam, 2013; Lo et al., 2010; Stam, Jones, Nolte, Breakspear, & Scheltens, 2006; Van Der Flier et al., 2002; Vlooswijk et al., 2011). There are several available imaging biomarkers for mild cognitive impairment (MCI) and AD including structural imaging markers, such as magnetic resonance imaging (MRI)-based hippocampal morphometry (Damoiseaux & Greicius, 2009; Jack et al., 1999; Jack et al., 2000; Tsao et al., 2017; Wang et al., 2011), molecular imaging markers, such as amyloid positron emission tomography (PET) (Johnson et al., 2013; Landau et al., 2012; Okello et al., 2009), and functional imaging markers, such as fludeoxyglucose (FDG)-PET (Caroli et al., 2012; Cohen & Klunk, 2014). Among these biomarkers, FDG-PET has been proven a precise predictor of both MCI and AD (Ito et al., 2015) and is more suitable to monitor disease progression because functional changes are presented in an early stage of the disease and continue to change as the disease progresses (Sheline & Raichle, 2013). However, FDG-PET uses ionizing radiation and is relatively expensive. As a noninvasive technique, resting-state functional magnetic resonance imaging (rs-fMRI) has been discussed as a functional imaging alternative for FDG-PET (Teipel et al., 2015). It evaluates low-frequency fluctuations in the blood oxygen level dependent (BOLD) signal while the subject is at rest, and is particularly useful in the setting for patients who are unable to cooperate with the task-based paradigm (Fox & Raichle, 2007; Lee et al., 2016). By measuring functional connectivity (FC) between spatially distinct brain regions, rs-fMRI can be used to evaluate brain functions (Biswal, Zerrin Yetkin, Haughton, & Hyde, 1995; Cordes et al., 2001). Although rs-fMRI is still investigational, some reports have indicated that this method is ready for clinical application in the preclinical setting (Lee, Smyser, & Shimony, 2013; Sheline & Raichle, 2013; Wang et al., 2013).

There are three general aspects/levels in AD-related research with fMRI modality, namely, regional coherence, functional connectivity, and functional network. Spontaneous low-frequency fluctuations (SLFF) (Biswal et al., 1995; Li et al., 2002), regional homogeneity (ReHo) (Zang, Jiang, Lu, He, & Tian, 2004), and amplitude of low-frequency fluctuations (ALFF) (Han et al., 2011; Liu et al., 2014) are among methods for the research of local regional coherence study. Such methods evaluate fMRI signal similarity or intensity for a given local region in the resting brain. However, the functional association between different regions cannot be obtained merely by such analyses. Thus, further functional connectivity analysis needs to be done on activated functional regions (Jiang & Zuo, 2016; Liu et al., 2008) by

methods including independent component analysis (ICA) (Beckmann, DeLuca, Devlin, & Smith, 2005), seed-based or region-of-interest (ROI) method (Poldrack, 2007), and so forth. Generally, the functional connectivity maps are then compared with a two-sample t test (Sheline & Raichle, 2013) which inevitably introduces the problem of mass-univariate hypothesis testing. To enable relatively comprehensive mapping of brain functional connectivity and topological organization, numerous studies have been focused on functional network (Biswal et al., 2010; He, Chen, Gong, & Evans, 2009; Wang et al., 2013; Wang, Zuo, & He, 2010) using various network analysis measures based on graph theory (Bullmore & Sporns, 2009; He & Evans, 2010; Sporns, 2011). With these measures, various nontrivial topological features, including small-world organization (Sanz-Arigita et al., 2010; Stam et al., 2006), modular structure (De Haan et al., 2012; Sporns & Betzel, 2016), and highly connected hubs (Binnewijzend et al., 2014; Dai et al., 2015), have been observed to be disrupted in MCI and dementia due to AD (Dai & He, 2014). The weighted networks usually require defining a set of thresholding values to remove spurious connections before quantifying network features (Giusti, Ghrist, & Bassett, 2016). The fixed thresholding scheme is a common practice to perform the selection of those strongest edges that exceed a given fixed threshold, which can be obtained based on the density of the network (Tong, Aganj, Ge, Polimeni, & Fischl, 2017), or using statistical criteria of connectivity strength (Binnewijzend et al., 2012; Smith & Nichols, 2009; Wang et al., 2013), and so forth. However, it may result in inconsistent network features when the thresholding value varies as its choice is rather arbitrary (Woo, Krishnan, & Wager, 2014; Zalesky, Cocchi, Fornito, Murray, & Bullmore, 2012). Therefore, the parameter-free scheme of cost thresholding has been applied to overcome this issue. The optimal thresholding value can be sought automatically by maximizing the cost efficiency (Khazaee, Ebrahimzadeh, & Babajani-Feremi, 2016), or keeping the shortest traveling paths (Dimitriadis et al., 2010) where minimum spanning tree (MST) (Stam et al., 2014) is an exemplar, and so on. However, such scheme usually only has one single optimal threshold, this operation may discard some potential valuable information during network construction (Giusti et al., 2016; Santarnecchi, Galli, Polizzotto, Rossi, & Rossi, 2014).

To address the issue of network threshold selection, a set of brain network analysis methods called *graph filtration* based on persistent homology (Chen & Edelsbrunner, 2011; Edelsbrunner & Harer, 2010; Wu et al., 2017) has been proposed to measure persistent brain network topology features generated over all possible thresholds (Choi et al., 2014; Chung, Hanson, Ye, Davidson, & Pollak, 2015; Lee et al., 2017; Lee, Kang, Chung, Kim, & Lee, 2012; Yoo et al., 2017). It quantifies various persistent topological features at different scales in a coherent manner and avoids the thresholding selection. Existing

approaches mainly associate persistent topological features, for example, the zeroth Betti numbers, with current varying thresholding values. However, they usually ignore the association between such features and forthcoming thresholding value changes to aggregate all connected components into one connected component. Imagine that there is an energy cost to consolidate individual brain networks into a fully connected component: we may name this feature the *connected component aggregation cost*. Intuitively, Betti numbers and aggregation cost are complementary, as Betti numbers describe invariant features in the current state, while the aggregation cost estimates the total cost for completing all subsequent evolutions in a nested filtration graph. Therefore, we propose a novel univariate and persistent brain network feature that considers both current and forthcoming persistent topological features and hypothesize that such a concise and persistent feature may boost statistical power to detect AD-induced topological changes in resting-state fMRI analysis.

In this article, we will develop a robust and parameter-free network measure, *Integrated Persistent Feature (IPF)* and apply it to study resting-state networks (RSN) constructed from rs-fMRI. In our experiments, we employ rs-fMRI data from the publicly available Alzheimer's Disease Neuroimaging Initiative (ADNI) to investigate the topological changes in the functional connectomes of patients of AD and MCI comparing with those of normal control (NC) subjects. Our data set consists of 106 subjects, including 31 AD, 38 MCI, and 37 NC subjects. We set out to test whether the proposed network feature provides a robust, computationally efficient, and statistically powerful measure of human brain network dynamics.

2 | METHODS

2.1 | Theoretic background

2.1.1 | Connected component aggregation cost

In a graph filtration (defined in Appendix A), the zeroth Betti numbers plot (BNP) (defined in Appendix B) shows how the number of connected components (i.e., the zeroth Betti number) varies over different filtration values (Ghrist, 2008). An example is shown in Figure 1. However, the zeroth Betti number only quantifies the invariant feature in a given state, and the state information of future networks (i.e., subsequent evolutional networks in a nested filtration graph) is not measured. Thus, we define an additional feature to quantify the
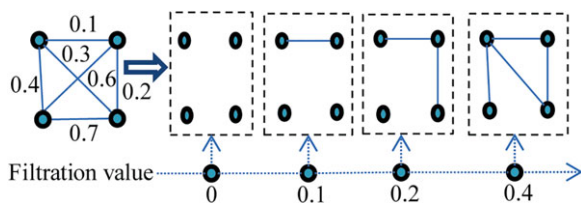

FIGURE 1 An example of graph filtration. The left is an original weighted graph X followed by four nested binary networks $\mathcal{B}(X,0) \subset \mathcal{B}(X,0.1) \subset \mathcal{B}(X,0.2) \subset \mathcal{B}(X,0.4)$ at four increasing filtration values 0, 0.1, 0.2, and 0.4, respectively [Color figure can be viewed at wileyonlinelibrary.com]

process for completing all subsequent evolutions in a nested filtration graph.

> **Definition 1:** We define connected component aggregation cost as the total of involved edge weights for completing all subsequent evolutions from any current connected components to a future fully connected component in a graph filtration. Given $\lambda_0 = 0$, as well as a tree T with $m \geq 2$ nodes and unique positive edge weights $\lambda_1 < \lambda_2 < \cdots < \lambda_{m-1}$, the connected component aggregation cost corresponding to the maximal graph filtration is defined as

$$l(T, \lambda_i) = \begin{cases} \sum_{k=i+1}^{m-1} \lambda_k, & 0 \leq i \leq m-2 \\ \\ 0, & i = m-1. \end{cases} \quad (1)$$

The connected component aggregation cost is defined as the summation of subsequent filtration values before evolving into a fully connected component on the collection of binary networks. The cost at filtration value λ_{m-1} is zero where all nodes are connected.

The connected component aggregation cost can be easily understood through energy consumption in the aggregation process from loose connected components to a fully connected component. Suppose each connected component has its energy and the energy will disappear once the component is connected with another. In other words, to connect more components, more energy consumption is required. In a graph filtration, none of the nodes is connected at the beginning when filtration value λ is zero; the nodes are gradually connected and eventually aggregate into one giant component when all nodes are connected. Thus, as we set the fully connected component as the target of graph evolution, the required energy consumption progressively declines with the graph evolution until all components are connected. In this way, because the graph filtration is produced by minimum spanning tree (Lee et al., 2012) in this study, the connected component aggregation cost can be thought as the least energy consumption for evolving from the current loose connected components to a future fully connected component.

To some extent, the connected component aggregation cost is related to path lengths between the connected components, as the more loosely connected the components are, the more aggregation cost will take to transit to more tightly connected components until all components are connected. As we know the changes in path lengths between nodes have been proved to be very important in brain network analysis (Braun, Muldoon, & Bassett, 2015), especially in AD research (Sheline & Raichle, 2013; Stam et al., 2006; Wang et al., 2013). We argue that the connected component aggregation cost may be a useful feature for the AD network analysis research.

2.1.2 | Integrated Persistent Feature

We further define a novel network measure, IPF, by integrating a prior topological feature (i.e., the zeroth Betti number) and the newly

defined connected component aggregation cost. The IPF without normalization can be defined as the product of $\beta_0(T, \lambda_i)$ and $l(T, \lambda_i)$,

$$\gamma'(T,\lambda_i) = \beta_0(T,\lambda_i) * l(T,\lambda_i) \qquad (2)$$

To confine the IPF between 0 and $\max(\lambda_i)$, we divide it by $m \times (m-1)$ and get a normalized form of IPF,

$$\gamma(T,\lambda_i) = \frac{\gamma'(T,\lambda_i)}{m(m-1)} \qquad (3)$$

Definition 2: According to Equations (1)–(3) and (B1), given $\lambda_0 = 0$, as well as a tree T with $m \geq 2$ nodes and unique positive edge weights $\lambda_1 < \lambda_2 < \cdots < \lambda_{m-1}$, the IPF corresponding to the maximal graph filtration is defined as

$$\gamma(T,\lambda_i) = \begin{cases} \dfrac{m-i}{m(m-1)} \sum\limits_{k=i+1}^{m-1} \lambda_k, & 0 \leq i \leq m-2 \\ \\ 0, & i = m-1 \end{cases} \qquad (4)$$

In Figure 2, we provide a topological feature computation example using the same data in Figure 1. The MST T of weighted graph X is constructed first. Then four nested binary trees $\mathcal{B}(T,0) \subset \mathcal{B}(T,0.1) \subset \mathcal{B}(T,0.2) \subset \mathcal{B}(T,0.4)$ are built at 4 increasing filtration values 0, 0.1, 0.2, and 0.4, respectively. According to Equations (B1), (1), (2), and (4), four topological features including the zeroth Betti number β_0, connected component aggregation cost l, non-normalized IPF γ', and IPF γ are computed.

The network structure can be detected by plotting the change of IPF over different filtration values when the connected component is evolving to form a bigger component. Previous BNP study only considers the changes in the number of connected components (Choi et al., 2014; Chung et al., 2015; Lee et al., 2012; Lee et al., 2017), while our proposed IPF plot encodes more evolutionary information of the connected components in graph filtration as the estimated information related to future state is also considered as the connected component aggregation cost. In brain network research, the IPF is usually limited between 0 and 1 as any correlation λ_i in a connectivity matrix is <1 normally. It enjoys an advantage that different numbers of nodes can be processed consistently. The following proposition provides the theoretical foundation for our proposed work.

Proposition 1: Given $\lambda_0 = 0$, as well as a tree T with $m \geq 2$ nodes and unique positive edge weights $\lambda_1 < \lambda_2 < \cdots < \lambda_{m-1}$, the IPF plot corresponding to the maximal graph filtration determined by each edge weight, λ, is a monotonically decreasing convergence function.

Please refer to Appendix C for its proof. Here our goal is to integrate the obtained multivariate IPF into a univariate network measure. According to Proposition 1, the IPF plot over all possible filtration values is a monotonically decreasing convergence function, so the IPF is also a persistent topology feature like the zeroth Betti number. Similar to the BNP plot methods (Choi et al., 2014; Chung et al., 2015; Lee et al., 2012; Lee et al., 2017; Yoo et al., 2017), we define the slope
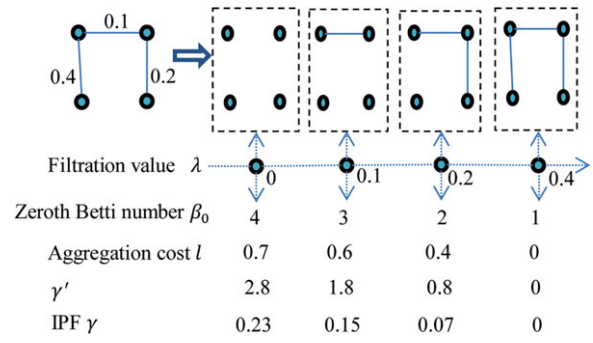

FIGURE 2 A computation example of topological features based on Figure 1. The top left is an MST T of weighted graph in Figure 1 left, followed by four nested trees $\mathcal{B}(T,0) \subset \mathcal{B}(T,0.1) \subset \mathcal{B}(T,0.2) \subset \mathcal{B}(T,0.4)$ at four increasing filtration values 0, 0.1, 0.2, and 0.4, respectively. The topological features of the binary network, such as the zeroth Betti number and IPF, are varied according to the increase of filtration value λ [Color figure can be viewed at wileyonlinelibrary.com]

of IPF plot (SIP) as a novel univariate network measure. When the filtration value λ evolves, the number of connected components is getting smaller and the connected component aggregation cost is getting less until all nodes are connected when the IPF is equal to zero. The proposed measure SIP may be thought as the information diffusion rate or the convergence speed of arriving to a fully connected component.

2.2 | Algorithms

Figure 3 shows the pipeline to measure and discriminate RSN structures with the proposed SIP measure. First, we use SPM8 toolbox, Data Processing Assistant for Resting-State fMRI (DPARSF) (Yan & Zang, 2010) and Resting-State fMRI Data Analysis Toolkit (REST) (Song et al., 2011) to preprocess the rs-fMRI data (the first row). Then we construct the single linkage distance matrix for each subject using SLD (Lee et al., 2012) according to correlation-based distance matrix from mean time series of predefined ROIs (the second row). We further compute IPF plots to measure constructed multiscale RSN based on persistent homology theory (the third row). With the goal to discriminate various AD diagnostic stages, the difference of RSN structures is evaluated by statistical group difference using our proposed method together with five other network measures over various parcellation schemes (the fourth row). We explain some major steps in the following subsections.

2.2.1 | Data acquisition and preprocessing

High-resolution brain scans were acquired at multiple ADNI sites using 3.0 T Philips MRI scanners. The rs-fMRI (Figure 3a) were obtained using an echo-planar imaging (EPI) sequence and the parameters included repetition time (TR) = 3,000 ms, echo time (TE) = 30 ms, flip angle = 80°, number of slices = 48, slice thickness = 3.3 mm, voxel size = 3 mm × 3 mm × 3 mm, voxel matrix = 64 × 64, and total volume = 140.

The preprocessing of rs-fMRI data (Figure 3b) was carried out using SPM8 toolbox (http://www.fil.ion.ucl.ac.uk/spm/), DPARSF (http://www.restfmri.net) (Yan & Zang, 2010), and REST (http://www.
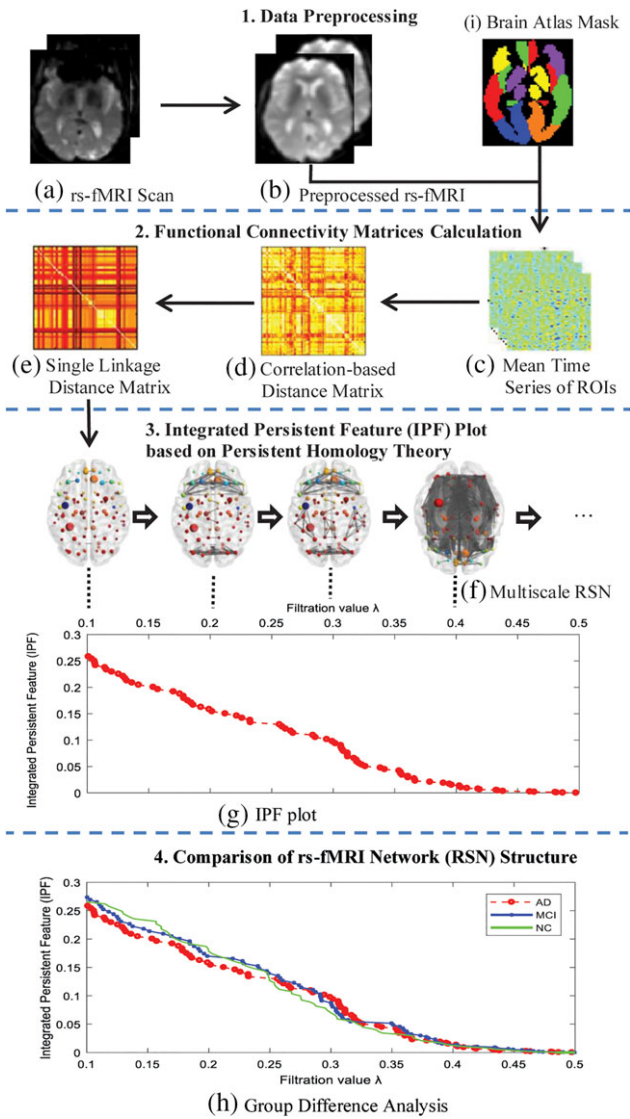
FIGURE 3 Pipeline to measure and discriminate RSN structures with the proposed SIP measure. (a) Each participant's rs-fMRI scan is preprocessed and normalized to the Montreal Neurological Institute (MNI) space (b), and the mean time series of ROIs are extracted (c). We calculate the observed distance matrix through Pearson correlation (d) and obtain the predicted distance matrix using single linkage dendrogram (SLD) (e). We further construct a multiscale RSN per subject from single linkage distance matrix (f) and plot the corresponding Integrated Persistent Feature (IPF) over different scales (g). We obtain all IPF plots and corresponding network measures of the slope of IPF plot (SIP), respectively, for all participants by repeating steps (a–g). The difference of RSN structures is evaluated by statistical group difference analysis (h) of our proposed measure together with five other network measures over various parcellation schemes (i) [Color figure can be viewed at wileyonlinelibrary.com]

restfmri.net) (Song et al., 2011) according to well-accepted pipelines. All subjects' data were preprocessed individually. Specifically, the first 10 acquired rs-fMRI volumes of each subject were initially removed prior to any further processing to stabilize the signal (Suk, Wee, Lee, & Shen, 2016). The remaining 130 volumes were then corrected for the staggered order of slice acquisition that was used during echo planar scanning to ensure the data on each slice correspond to the same point in time. The images were realigned with the image at the time

point of TR/2 (slice# 47) as reference to minimize relative errors across each TR. After correcting acquisition time delay, the volumes of each subject were realigned to its mean image based on rigid body transformation and least squares techniques, and spatially normalized to the Montreal Neurological Institute (MNI) space. Subsequently, all images were spatially smoothed with a Gaussian kernel of $4 \times 4 \times 4$ mm^3 full-width at half-maximum, then linear trend adjustments were performed. It has been shown that a frequency range between 0.025 and 0.06 or 0.07 is reliable for test–retest experiments (Liu et al., 2014; Malinen et al., 2010; Xi et al., 2012). In this regard, the functional time series data were band-pass filtered to retain frequencies between 0.01 and 0.08 Hz, which is the relevant frequency range. To further reduce the effects of nuisance signals (Weissenbacher et al., 2009) and focus on the signals of gray matter, a validated confound regression procedure (Van Dijk et al., 2010) was performed on each subject's time series data to remove confounding factors including cerebrospinal fluid signals and white matter signals as well as six head-motion profiles. Due to the ongoing controversy of removing the global signal in the processing of rs-fMRI data (Fox, Zhang, Snyder, & Raichle, 2009; Murphy, Birn, Handwerker, Jones, & Bandettini, 2009), we omitted the process of global signal regression (Lynall et al., 2010; Supekar, Menon, Rubin, Musen, & Greicius, 2008). In addressing head motion concerns in resting-state fMRI analyses (Power, Barnes, Snyder, Schlaggar, & Petersen, 2012; Satterthwaite et al., 2013; Van Dijk, Sabuncu, & Buckner, 2012), we assessed the rotation and translation for all subjects and excluded subjects with excessive head motion with a displacement of more than 1 mm or an angular rotation of more than 1° in any direction.

2.2.2 | Multiscale network reconstruction by SLD

First, we use the Pearson correlation to construct RSN. We extract the time series of rs-fMRI signals (Figure 3c) from n selected ROIs and each ROI serves as a node in the brain network. The measurement set is denoted as $X = \{x_1, x_2, \cdots, x_n\}$ where x_i represents a time series at ith node. We define the *observed distance* (Figure 3d) between the measurements x_i and x_j through the Pearson correlation,

$$w_X(x_i, x_j) = 1 - \mathrm{corr}(x_i, x_j) \tag{5}$$

Here, corr(x_i, x_j) is the Pearson correlation function. A stronger functional connectivity infers a higher Pearson correlation corr(x_i, x_j), producing the shorter observed distance, that is, the lower edge weight $w_X(x_i, x_j)$. In the graph filtration, the lower edges with stronger functional connectivity are added first to better reflect true biological connections. After the weighted matrix $\{w_X(x_i, x_j)\}$ of each subject is constructed as functional connectivity network, we reconstruct the multiscale network as described below.

The filtered subnetworks on top of the weighted network should be built before computing the persistent features of the complex, according to a typical workflow of persistence in topological data analysis (Chazal, Glisse, Labruere, & Michel, 2013). The most intuitive approach is to sort all weights of original network in ascending order and use the ranks as indices for the subnetworks (Petri et al., 2014). The computation of such an approach is less efficient especially for high-resolution networks, and a common practice is to limit the size of filtrations by equally dividing maximum weights (Adams, Tausz, &

Vejdemo-Johansson, 2014). However, it requires selecting a number of nested subgraphs empirically. In this study, the representative filtrations are generalized in an unbiased manner by the single linkage cluster analysis (Gower & Ross, 1969) as a convenient way of summarizing taxonomic relationships in the form of dendrograms. This SLD involves defining a single linkage distance as the model predicted distance (Lee et al., 2012) (Figure 3e). Let $p = \{v_0, v_1, \cdots, v_k\} \in P$ be a path between x_i and x_j, where P is the collection of all possible paths between x_i and x_j, and $v_0 = x_i$, $v_k = x_j$. The single linkage distance is formally defined as below.

$$d_X(x_i, x_j) = \min_{\forall p \in P} \left[\max_{l=0,\cdots,k-1} w_X(v_1, v_{l+1}) | p = \{v_0, v_1, \cdots, v_k\} \right] \quad (6)$$

It denotes the shortest distance of all maximum edges over every possible path between any specific pair of nodes. Given a weighted network X with edge weight matrix $\{w_X(x_i, x_j)\}$, we can get the single linkage distance matrix $\{d_X(x_i, x_j)\}$ and sort it in the ascending order $\{\lambda_1, \lambda_2, \cdots\}$. The SLD method initially treats each node as a cluster and iteratively merges two closest clusters at each step. Two clusters will combine when at least there exists one link between them of length λ where $\lambda_i < \lambda < \lambda_{i+1}$. The dendrogram shows how clusters at level λ_1 combine at level λ_2 and so on at successive levels until all clusters combine into a single cluster at the root of the tree.

Similar to the SLD method (Gower & Ross, 1969), the zeroth persistent homology graph filtration is used to analyze a family of graphs and requires hierarchically building nested structures (Giusti et al., 2016). All components are initially born and more and more components are disappeared once they are connected when we gradually increase the filtration values. We can generate graph filtrations by the SLD method which is equivalent to building the MST (Murtagh, 1983) as the clusters at any level λ_i can be obtained from the MST by deleting all segments of length $>\lambda_i$. Therefore, each level of filtered network at λ_i is used as a single scale under the original weighted network, and further the corresponding persistent feature IPF at such scale can be computed (Equation (4)). By summarizing the network topology of all scales, we can investigate spatial dynamics of RSN.

It should be noticed that our multiscale framework is different from some existing MST analyses on brain network analysis (Stam et al., 2014; Tewarie, van Dellen, Hillebrand, & Stam, 2015; Van Dellen et al., 2014; Van Dellen et al., 2018). First of all, the purposes of using MST are different. The goal of existing studies (Stam et al., 2014; Tewarie et al., 2015; Van Dellen et al., 2014; Van Dellen et al., 2018) is to investigate the conventional graph theoretical features on MST directly, such as diameter, leaf fraction, and centrality, and then study their differences between health and illness. In contrast, we use MST to build a set of thresholds (filtration values) for graph filtration in an unbiased manner and the persistent features over all thresholding nested subnetworks are then quantified. Second, exiting MST studies usually focus on the features computed at one fixed scale of MST based on graph theory, while we investigate the spatially dynamic evolutions in different scales. Last, a tree without forming loops is also a much simpler structure than the nested filtered subnetworks. However, existing MST studies cannot reflect some properties that depend upon cycles. Theoretically speaking, they may be detected by our framework when we extend the persistent dimension

from the zeroth Betti number, β_0, to the first Betti number, β_1, in future.

2.2.3 | Statistical group difference analysis

In this study, the brain network is constructed at macroscale where nodes represent brain regions and edges represent interregional FC at resting state. To define network nodes, we divide the brain into 90 ROIs according to a low-resolution automated anatomical labeling atlas (L-AAL90) (Tzourio-Mazoyer et al., 2002). We calculate Pearson correlation-based distance w_X according to Equation (5) between the representative time series of each node extracted from each subject and get 90×90 symmetric FC matrices. After producing a single linkage distance matrix per subject according to Equation (6), the multiscale RSN is constructed using our proposed methods for every subject in AD, MCI, and NC groups by graph filtration, and the corresponding SIP is obtained.

Here our proposed SIP is used as a univariate feature for statistically characterizing network differences. In contrast to previous work that produces one multiscale network per group (Choi et al., 2014; Chung et al., 2015; Lee et al., 2012; Lee et al., 2017), we construct one network per subject to improve the ease of use and computation efficiency. For subject i in group 1, we construct a multiscale network (Figure 3f) and its MST T_i by SLD, subsequently corresponding IPF $\gamma^1(T_i, \lambda)$ (Figure 3g) is computed with Equation (4). For subject j in group 2, we can also generate a multiscale network and MST T_j as well as IPF $\gamma^2(T_j, \lambda)$ in the same way. Although we are interested in testing whether the IPF plots are different between groups, we do not intend to directly set the pointwise null hypothesis as

$$H'_0 : \text{mean}\left(\gamma^1(T_i, \lambda)\right) = \text{mean}\left(\gamma^2(T_j, \lambda)\right) \text{ for all } \lambda \in [0, 1],$$

because it will perform multiple comparisons of IPF at different filtration values. Instead, we compare the proposed network measure SIP. Given the ith subject's SIP in Group 1 and jth subject's SIP in Group 2 are represented as α_i^1 and α_j^2, the null hypothesis is

$$H_0 : \text{mean}\left(\alpha_i^1\right) = \text{mean}\left(\alpha_j^2\right), \quad (7)$$

while the alternate hypothesis is

$$H_1 : \text{mean}\left(\alpha_i^1\right) \neq \text{mean}\left(\alpha_j^2\right),$$

where mean is the average of SIPs in a group.

As there is no prior study on the statistical distribution of SIP, it is difficult to construct a parametric test procedure. Moreover, the sample is limited, so it is necessary to empirically construct the null distribution and determine the p value. In this study, we carry out two kinds of nonparametric statistical analyses (Figure 3h). First, between-group differences of AD versus MCI, AD versus NC, and MCI versus NC are inferred according to Equation (7) by nonparametric permutation test with 10,000 permutations (Wang et al., 2013; Yao et al., 2010), which has been usually used in pairwise comparisons in network measures. Then we execute the Kruskal–Wallis test (Hollander, Wolfe, & Chicken, 1973) for detecting multi-group difference among three groups of AD versus MCI vrersus NC.

2.2.4 | Reproducibility and test–retest reliability

Graph-based brain connectome analyses are usually sensitive to the choice of brain parcellation schemes (Bai et al., 2009; Biswal et al., 1995; Buldú et al., 2011; Wang et al., 2009). To evaluate the reproducibility and test–retest reliability, we evaluate our methods against different parcellation schemes. We define network nodes with five brain atlases with different resolutions, including four low-resolution atlases of automated anatomical labeling atlas with 90 ROIs (L-AAL90) and 116 ROIs (L-AAL116) (Tzourio-Mazoyer et al., 2002), Harvard-Oxford atlas with 112 ROIs (L-HOA112) (Kennedy et al., 1998; Makris et al., 1999), and Craddock et al. functional atlas with 200 ROIs (L-Crad200) (Craddock, James, Holtzheimer, Hu, & Mayberg, 2012), as well as one randomly generated high-resolution atlas with 1,024 ROIs (H-1024) (Zalesky et al., 2010). The statistical group difference analysis (Figure 3h) of our proposed method together with five other measures are evaluated and compared under all five parcellation schemes (Figure 3i).

3 | RESULTS

We conducted two experiments to verify our proposed network measure with some synthetic data and the ADNI rs-fMRI data. For replicating our results, we have provided our experimental data and MATLAB source code at http://gsl.lab.asu.edu/software/IPF.

3.1 | Synthetic data results

We conducted two sets of synthetic data studies to evaluate our method performance for brain connectivity analysis and test–retest reliability studies.

In the first synthetic data experiment, the simulated brain data of three groups were generated randomly. Each group has $K = 40$ subjects and each subject has $S = 100$ volumes of scanning images. There are $M = 90$ nodes representing brain ROIs defined by L-AAL90 atlas. The initial data of $x_{ijk}, y_{ijk}, z_{ijk}$ in three groups at node j for subject k at ith volume were simulated as independent standard normal $N(0, 1)$ respectively. Here the normal distribution is defined as $N(\mu, \sigma) = \frac{1}{\sqrt{2\pi\sigma^2}}e^{-\frac{(x-\mu)^2}{2\sigma^2}}$ where μ is the mean and σ is the standard deviation. Then we added small noise $N(0, 0.01–0.1)$ into y to make x and y are not exactly the same. To simulate connected components in each group, we selected four nodes indexed by $p = 1, 3, 5, 7$ for first two groups, and eight nodes indexed by $p = 1, 3, 5, ... 15$ for the third group. These eight nodes represent 8 left hemisphere brain regions defined in L-AAL90 respectively, that is, precentral gyrus, superior frontal gyrus, superior frontal gyrus (orbital part), middle frontal gyrus, middle frontal gyrus (orbital part), inferior frontal gyrus (pars opercularis), inferior frontal gyrus (pars triangularis), and inferior frontal gyrus (pars orbitalis). After that, extra linear dependencies were introduced into x, y, z, respectively, to increase correlations between all selected nodes. Specifically, the synthetic data are defined as below:

$$\text{Group } 1: \begin{cases} x_{ijk} = N(0,1) \\ x_{ipk} = 0.1\,x_{i1k} + N(0,0.01) \end{cases}, p \in (A = \{3,5,7\}),$$

$$\text{Group } 2: \begin{cases} y_{ijk} = N(0,1) + N(0,0.1) \\ y_{ipk} = 0.1\,y_{i1k} + N(0,0.01) \end{cases}, p \in (A = \{3,5,7\}), \qquad (8)$$

$$\text{Group } 3: \begin{cases} z_{ijk} = N(0,1) \\ z_{ipk} = 0.1\,z_{i1k} + N(0,0.01) \end{cases}, p \in (A = \{3,5,7,\cdots,15\}),$$

where $i \in \{1, 2, ..., S\}, j \in \{1, 2, ..., M\} \backslash A, k \in \{1, 2, ..., K\}$.

Note that we also added small noise $N(0, 0.01)$ to perturb the node values. In the end, correlation matrices based on the synthetic brain data were obtained by Pearson correlation (Equation (5)).

Following the proposed methods, we obtained 40 multiscale brain networks and corresponding SIPs in each group. Randomly selected examples of synthetic multiscale networks are shown in Figure 4. Then permutation tests were applied according to Equation (7) and we obtained the mean p values of 0.52 and $1.6e^{-5}$ over 2000 simulations for Group 1 versus Group 2, and Group 2 versus Group 3, separately. As Groups 1 and 2 have the same size of connected components with high correlations, we could not detect any group difference. There is a significant difference between Groups 2 and 3 as they have different sizes of connected components. Figure 5 shows the results of the group difference study with synthetic data. The IPF gradually decreases and one fully connected component is constructed eventually while changing filtration value from 0 to 1. The SIP in group 3 is not as steep as those in Groups 1 and 2, while Groups 1 and 2 have similar steepness (Figure 5a). The group differences could be detected intuitively from the resulting SIPs in Figure 5b where all 40 subjects' SIPs of each group are exhibited. The significance corresponds to the vertical gap between the SIPs. There is no significant group difference between Groups 1 and 2 ($p = .52$), comparing to significant differences in Group 2 versus 3 and Group 1 versus 3 ($p = 1.6e^{-5}$ for both).

In the second synthetic data experiment, for the purpose of test–retest reliability study, we changed the number of nodes from 90 to 50, 150, 250, 350, 500, 800, and 1,000 under different subject number of 20, 40, 60, 100, and 200, respectively. Then we test–retested the synthetic multiscale brain networks according proposed methods over 100 times. There is still no significant difference between Groups 1 and 2 ($p > .31$), comparing to the significant differences in Group 2 versus 3 and Group 1 versus 3 ($p < .0001$ for both) as expected.

3.2 | Application to AD

With rs-fMRI data, using the predefined 90 ROIs, we constructed multiscale brain networks using our proposed methods. Group differences were studied by the SIP with the subject-wise network. Finally, we evaluated our proposed method under four additional brain parcellation schemes with 112, 116, 200, and 1,024 ROIs. We compared the new measure with another persistent homology-based measure (BNP) and four widely used graph theory approaches that characterize the brain network topologic features of small-world organization, modular structure, and highly connected hubs.
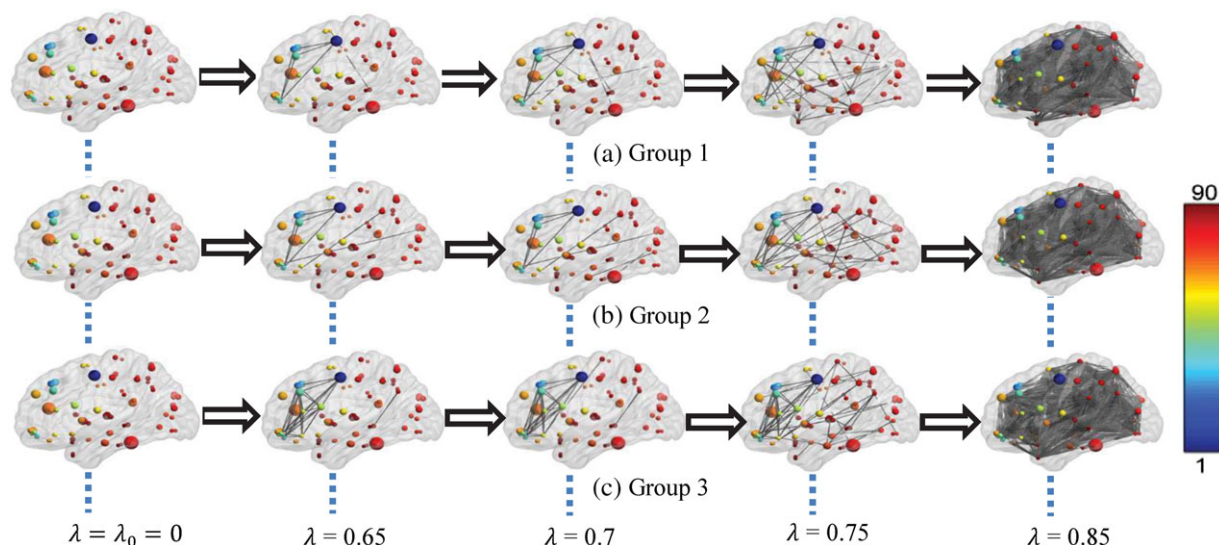
FIGURE 4 The synthetic multiscale brain networks at five different filtrations values 0, 0.65, 0.7, 0.75, and 0.85 for Groups 1, 2, and 3 with 4, 4, and 8 highly connected nodes, respectively. The color of nodes represents the node index predefined in L-AAL90 atlas. Specifically, the eight selected nodes indexed by p = 1, 3, 5, …, 15 represent 8 left-hemisphere brain regions defined in L-AAL90, respectively. They are precentral gyrus, superior frontal gyrus, superior frontal gyrus (orbital part), middle frontal gyrus, middle frontal gyrus (orbital part), inferior frontal gyrus (pars opercularis), inferior frontal gyrus (pars triangularis), and inferior frontal gyrus (pars orbitalis) [Color figure can be viewed at wileyonlinelibrary.com]

3.2.1 | Subjects

Data used in the preparation of this article were obtained from the ADNI database (adni.loni.usc.edu). The ADNI was launched in 2003 as a public–private partnership, led by Principal Investigator Michael W. Weiner, MD. The primary goal of ADNI has been to test whether serial MRI, PET, other biological markers, and clinical and neuropsychological assessment can be combined to measure the progression of MCI and early AD.

At the time of downloading from ADNI database (May, 2017), there were 31 AD patients aged 60–90 years in the rs-fMRI dataset. They were matched by age, gender, and education to 38 MCI and 37 NC subjects, together comprising the 106 participants selected for

this study. These subjects had been recruited from 15 sites across the U.S. and Canada, and only their first valid rs-fMRI was selected for this study. In Table 1, we present their detailed demographic information. All studied images had no excessive head motion (six-parameter rigid body) defined by a displacement of <0.7 mm or an angular rotation of less than in any direction $0.8°$. The Kruskal–Wallis tests (Hollander et al., 1973) showed no significant differences in gender, age, education, or head motion among the AD, MCI, and NC groups, while there were significant differences in Mini-Mental Status Examination (MMSE) scores (Folstein, Folstein, & McHugh, 1975) and Clinical Dementia Rating (CDR) global scores (Morris, 1993). Diagnostic classification was made by ADNI investigators using established criteria
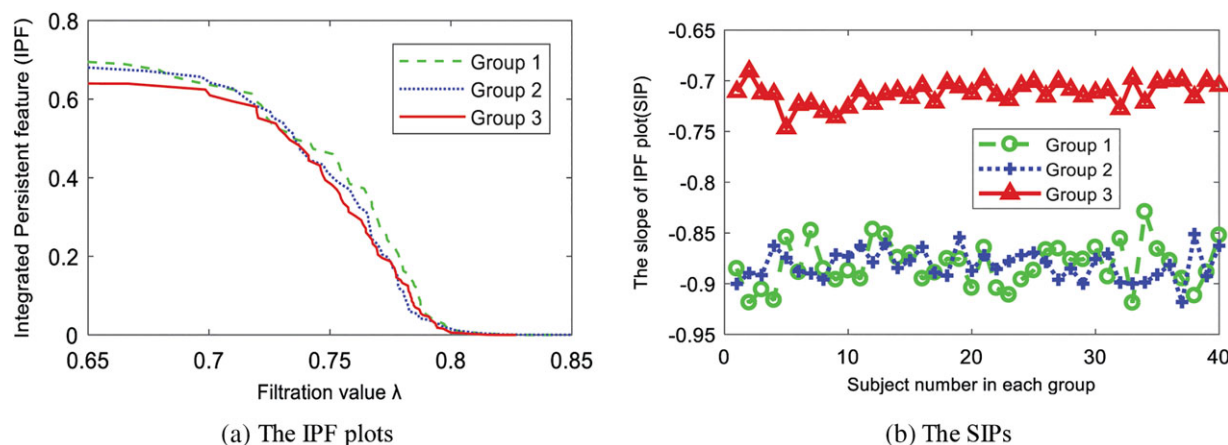

(a) The IPF plots

(b) The SIPs

FIGURE 5 The synthetic data results of group difference study. (a) The resulting Integrated Persistent Feature (IPF) plots imply group differences. The IPF gradually decreases and one fully connected component is constructed eventually while changing filtration value from 0 to 1. The SIP in group 3 is not as steep as those in group 1 and 2, while group 1 and 2 get similar steepness. (b) The resulting SIPs for all 40 subjects of each group showing group differences. The significance corresponds to the vertical gap between the SIPs. There is no significant group difference between group 1 and 2 (p = .52), comparing to significant difference in group 2 versus 3 and group 1 versus 3 (p = **1.6e^{-5}** for both) [Color figure can be viewed at wileyonlinelibrary.com]

TABLE 1 Demographical information of the subjects[a]

	AD (n = 31)	MCI (n = 38)	NC (n = 37)	p value
Age (years)	60.7–86.6 (74.0±6.1)	60.0–88.7 (73.1±7.3)	65.2–90 (74.1±6.2)	.7486
Education (years)	0–20 (15.4±3.9)	11–20 (15.6±2.9)	0–20 (16.1±3.6)	.4267
Gender (male/female)	16/15	19/19	15/22	.6033
Head translation (mm)	0.13–0.70 (0.31±0.12)	0.13–0.62 (0.32±0.14)	0.07–0.60 (0.31±0.12)	.9895
Head rotation (°)	0.09–0.77 (0.30±0.17)	0.10–0.59 (0.25±0.13)	0.08–0.51 (0.25±0.11)	.3083
MMSE	22.8±3.4 (17–26)	27.8±1.5 (26–30)	28.8±1.6 (25–30)	.0015
CDR (global score)	≥1	0.5	0	–

[a] Data are presented as the range of minimum–maximum (mean±SD). The p value was obtained using the Kruskal–Wallis test (Hollander et al., 1973) by R software (Team, 2014).

(McKhann et al., 1984; McKhann et al., 2011; Petersen et al., 2001). NC had MMSE scores between 25 and 30, no significant memory concerns, and CDR global scores of 0. MCI patients had MMSE scores between 26 and 30, and a CDR score of 0.5. Participants in the AD cohort had MMSE scores between 17 and 26, and fulfilled the NINCDS-ADRA (National Institute of Neurological and Communicative Disorders and Stroke and the Alzheimer's Disease and Related Disorders Association) criteria for probable AD (Makedonov, Chen, Masellis, & MacIntosh, 2016).

3.2.2 | Multiscale network and corresponding SIP

We constructed weighted matrices for all subjects by Equation (5) where the observed distance w_x is one minus correlation. Although w_x is always between 0 and 2 and may have a value larger than 1, all nodes are connected before w_x reaches 1 in our current dataset during the graph filtration. Thus, the filtration is finished when w_x between 0 and 1. To observe the group differences among AD, MCI,

and NC, we further constructed the mean RSN for each group which is an average of all involved subject's networks. Figure 6 shows three multiscale RSNs at 6 different values 0.1, 0.15, 0.2..., 0.35 computed from three group means of brain networks. We found that the connected components in NC aggregated faster than MCI, and much faster than AD. The topological changes in the number of connected component for 3 group mean RSNs were visualized by the SLD in Figure 7. We calculated the corresponding IPF of three group means under the multiscale RSN at all different filtration values, and showed the relationship between filtration values and IPFs in Figure 8. Our proposed IPF not only considers the changes in the number of connected component, but also introduces an extra connected component aggregation cost at the same time (Equation (4)). The IPF gradually decreases and one fully connected component is constructed eventually when filtration values vary from 0 to 1. We found that the SIP of NC group mean is steeper than MCI's and much steeper than AD's.
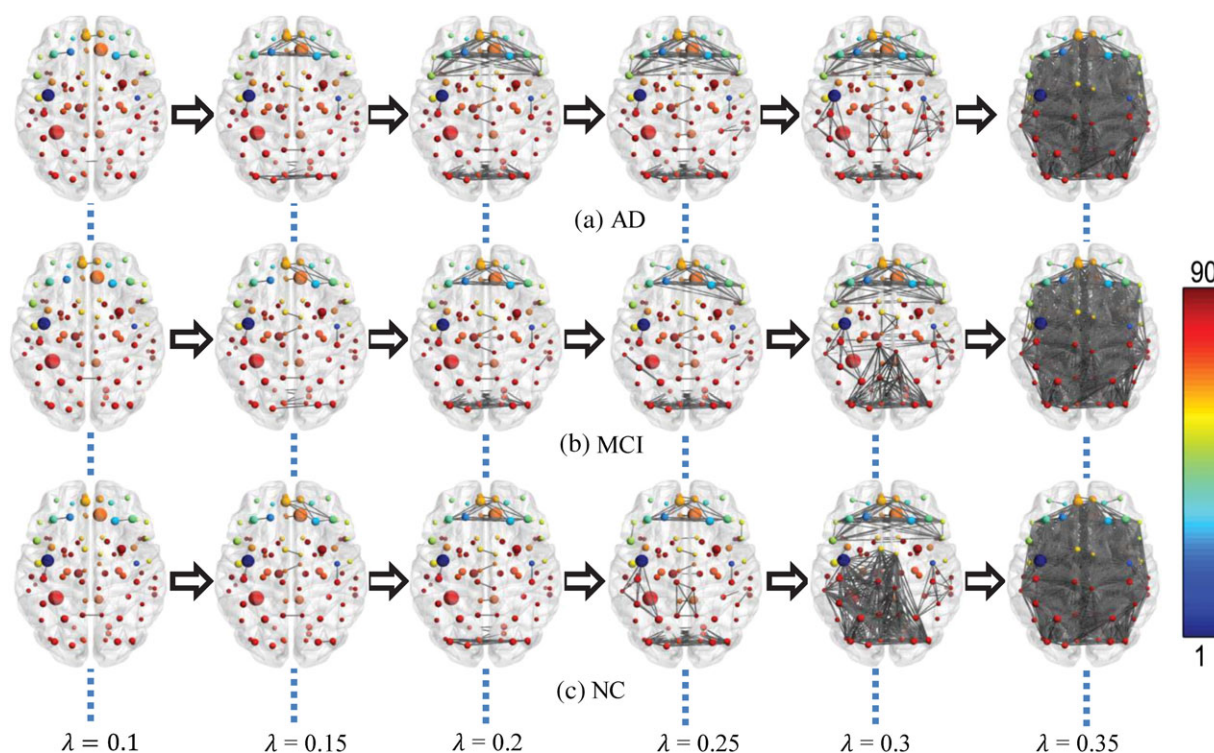

FIGURE 6 The constructed multiscale brain networks using our proposed methods for 3 group means of (a) AD, (b) MCI, and (c) NC at 6 different filtrations values 0.1, 0.15, 0.2, ..., 0.35. The color of nodes represents the node index predefined in L-AAL90 atlas [Color figure can be viewed at wileyonlinelibrary.com]
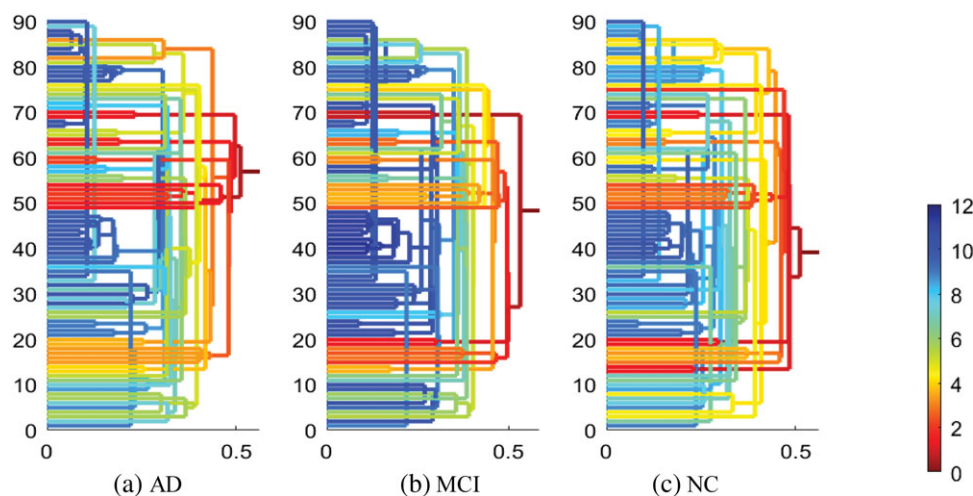
FIGURE 7 The single linkage dendrograms (SLDs) for 3 group means of (a) AD, (b) MCI, and (c) NC. The vertical and horizontal axes represent the node index and filtration value, respectively. The color of lines represents the total edge weight from current connected component to the giant component. The total weight from the giant component is 0. When individual components evolves to a fully connected component, the total edge weight decrease [Color figure can be viewed at wileyonlinelibrary.com]

3.2.3 | Statistical group difference analysis

We compared our work with another persistent homology-based method of BNP (Chung et al., 2015; Lee et al., 2012; Lee et al., 2017) and four other widely used graph measures that summarize global network topology. Numerous studies (Bullmore & Sporns, 2009) have confirmed that both structural as well as functional brain networks display the typical features of a small-world organization, modular structure, and highly connected hubs, whose exemplars are the characteristic path length (CPL) (Brier et al., 2014; Watts & Strogatz, 1998), modularity (Mod) (Sporns & Betzel, 2016; Tagliazucchi et al., 2013), and eigenvector centrality (EC) (Binnewijzend et al., 2014; Qiu et al., 2016; Van Duinkerken et al., 2017), respectively. Thus we compared our work with these three measures and network diameter (ND) (Assenov, Ramírez, Schelhorn, Lengauer, & Albrecht, 2007; Fagerholm, Hellyer, Scott, Leech, & Sharp, 2015) as the path is important for functional network analysis. Specifically, the characteristic path length is the average shortest path length between all pairs of nodes in the graph, indicating how easily information can be transferred across the network (Rubinov & Sporns, 2010), while the modularity measures how the network can be subdivided into modules or communities (Newman & Girvan, 2004; Tagliazucchi et al., 2013). The nodal eccentricity is the greatest geodesic distance between the node and any other nodes (Assenov et al., 2007; Hage & Harary, 1995). It can be thought of as how far a node is from the node most distant from it in the graph. The network diameter is the maximum eccentricity of any node in the network, that is, the greatest distance between any pair of nodes (Hage & Harary, 1995). Furthermore, eigenvector centrality (Van Duinkerken et al., 2017) is a self-referential measure that assigns a high level of importance to nodes if they are connected to other nodes that are themselves highly connected. The eigenvector centrality of a node is decreased if its neighbors lose connectivity with their local hubs (Binnewijzend et al., 2014; Fagerholm et al., 2015). We adopted the Brain Connectivity Toolbox (BCT, https://sites.google.com/site/bctnet/) (Rubinov & Sporns, 2010) for their implementation. For a fair comparison, similar to a prior study (Wang et al., 2013) in threshold selection of weighted network, we retained the network matrix elements whose corresponding p values passed through a statistical threshold (Bonferroni corrected $p < .05$) for each correlation matrix in graph measures of CPL, ND, EC, and Mod.
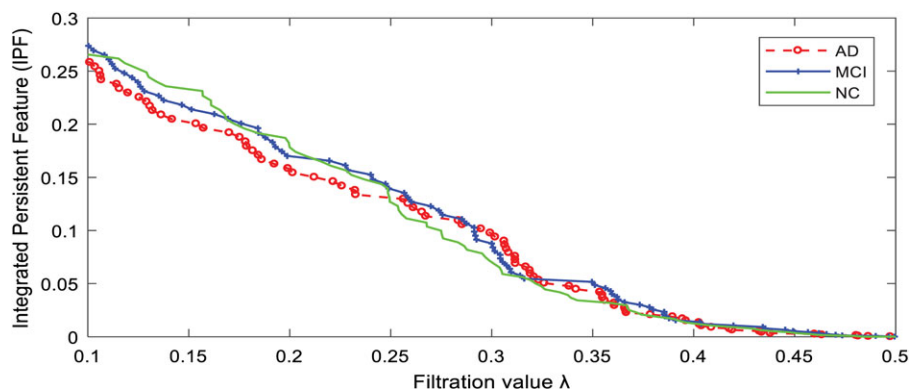

FIGURE 8 The resulting Integrated Persistent Feature (IPF) at different filtration values for 3 group means of (a) AD, (b) MCI, and (c) NC. Their SIPs are −0.71, −0.73, and − 0.77, respectively [Color figure can be viewed at wileyonlinelibrary.com]

TABLE 2 Between-group differences of different network measures over L-AAL90 atlas

	Network measure					
Between-group	SIP	BNP	CPL	ND	EC	Mod
AD vs MCI	**0.046**[a]	0.499	0.391	0.415	0.088[c]	0.497
AD vs NC	**0.0006**[b]	0.016[a]	0.203	0.097[c]	0.046[a]	0.153
MCI vs NC	0.033[a]	**0.011**[a]	0.094[c]	0.099[c]	0.311	0.098[c]
AD vs MCI vs NC	**0.002**[b]	0.073[c]	0.614	0.559	0.500	0.800

Threshold selection: The first two measures are threshold-free, while the last four measures take the significant network edges by Bonferroni correction method with corrected *p* value <.05.

Measures: proposed SIP, slope of IPF plot; BNP, the zeroth Betti numbers plot (Chung et al., 2015; Lee et al., 2012; Lee et al., 2017); CPL, characteristic path length (Brier et al., 2014; Wang et al., 2013); ND, network diameter (Assenov et al., 2007; Fagerholm et al., 2015); EC, eigenvector centrality (Binnewijzend et al., 2014; Qiu et al., 2016); Mod, modularity (Sporns & Betzel, 2016; Tagliazucchi et al., 2013).

The *p* value was obtained using 10,000 permutation test between two single groups and Kruskal–Wallis test (Hollander et al., 1973) for multiple comparisons among all three groups by R software (Team, 2014), respectively. The minimum *p* value in each row is bold.

[a] $.01 \leq p \leq .05$.
[b] $p < .01$.
[c] $.05 < p < .1$.

The acquired *p* values of our proposed SIP and other network measures are shown in Table 2. Our proposed SIP can detect differences from any two groups at the 0.05 level and three groups at the 0.01 level (*p* = .002). It achieved greater statistically significant group differences compared to another persistent homology-based method of BNP (Chung et al., 2015;Lee et al., 2012 ; Lee et al., 2017) which cannot detect significant differences between AD and MCI groups at the 0.05 level (*p* = .499). In addition, prior research (Chung et al., 2015) indicated that it is impractical to study group difference analysis by permutation test of 10,000 permutations because it would take about 7 days of computation in their experimental environment. We evaluated it in our experimental environment and confirmed that our method requires much less computation than the previous method (Chung et al., 2015) which requires converging all original image sets to construct group-wise networks in a round of permutation (about 0.84 s) and requires about 2.3 h (10,000 × 0.84 s) for the entire testing process. In our setup, since the subject-wise RSN is constructed one time (about 0.48 s) and corresponding network feature SIP that is used for permutation test can be obtained beforehand, the computation is mainly used to calculate SIP for all subjects. Thus it only took about 270 s (106 × 0.48 s plus some additional test time) for 106 subjects in all 10,000 permutation test. It is roughly a 31-fold efficiency gain in our current dataset.

Furthermore, we also compared our work with four traditional graph measures that summarize global network topology of small-world organization, modular structure, and highly connected hubs, including CPL, ND, EC, and Mod. The acquired *p* values of these measures are shown in Table 2. We can find that our propose SIP obtained better significance of group difference, and only our proposed method can detect difference among three groups at significance level of *p* < .01 (Table 2) in the current dataset. It implies that our method may have stronger statistical power in discriminating different AD diagnostic stages in the population-based studies.

In general, our experimental results show that our proposed SIP achieved more significant group difference in our dataset. The newly added connected component aggregation cost possibly played an important role as it is related to path length between the connected components to some extent, which is very important in AD patients as their path lengths exhibit apparent changes (Sheline & Raichle, 2013; Stam et al., 2006; Wang et al., 2013).

3.2.4 | Reproducibility and test–retest reliability analysis

Graph-based brain connectome analyses are sensitive to the choice of parcellation schemes (Bai et al., 2009; Biswal et al., 1995; Buldú et al., 2011; Wang et al., 2009). To assess the effects of different parcellation strategies, we carried out the same set of analyses with four other commonly employed atlases, including three low-resolution atlases of L-HOA112 (Kennedy et al., 1998; Makris et al., 1999), L-AAL116 (Tzourio-Mazoyer et al., 2002), and L-Crad200 (Craddock et al., 2012), as well as a randomly generated high-resolution atlas H-1024 (Zalesky et al., 2010). The detailed statistical significances of group difference under subject-wise networks are presented in Table 3, which shows that our proposed SIP achieved better robustness across different parcellation schemes.

4 | DISCUSSION

This study has three main findings. First, we generalize the BNP methods (Chung et al., 2015; Lee et al., 2012; Lee et al., 2017) by proposing a novel network measure, SIP, which integrates the zeroth Betti number and the newly defined connected component aggregation cost to reflect some complementary information related to the forthcoming state in the process of graph evolution. Our theoretical proof shows its feasibility and empirical experiments results demonstrate that our approach may improve statistical power and enjoy stronger parcellation robustness. Second, we adapt multiscale brain network construction from group-wise to subject-wise by statistical inference and thus improve the computation efficiency for large-scale brain network analyses. By constructing subject-wise multiscale networks, we showed that our methods gained strong efficiency in the case of permutation test with 10,000 permutations. Third, we studied the performance of our newly defined measure in the ADNI data set while previous studies of persistent homology mainly analyzed FDG-PET and structural MRI data for other diseases, such as epilepsy (Choi et al., 2014), autism spectrum disorder, and attention-deficit hyperactivity disorder (Lee et al., 2012; Lee et al., 2017). To our knowledge, it

is the first time that persistent homology has been applied to analyze RSN for AD research. Our work offers some new insights to RSN changes related to AD progression and may provide evidence for the RSN-based noninvasive preclinical AD imaging biomarker research.

4.1 | Subject-wise versus group-wise network

The multiscale RSN was constructed using an ROI-based approach with 90 ROIs at all possible filtration values. There are two kinds of networks, that is, subject-wise network and group-wise network. The subject-wise network is an ROI-connectivity network produced from a single subject, while the group-wise network is an average of all involved subject-wise networks. In this study, we performed the statistical hypothesis testing directly over the original subject-wise network, rather than the more easily detectable group-wise network by jackknife resampling method that Chung and his coauthors applied in their seminal persistent homology-based studies (Chung et al., 2015; Lee et al., 2012; Lee et al., 2017). Intuitively, the between-group differences in group-wise networks should be easier to detect than that in subject-wise networks. We may apply bottleneck distance to quantify the difference between two networks. This metric is often used in

measuring the distance between two networks in the same metric space (Edelsbrunner & Harer, 2010). The bottleneck distance between two networks X and Y with the same node sets $V=\{v_0, v_1, \cdots, v_k\}$ is defined as

$$d_B(X,Y) = \min_{\forall v_i \in V} \max_{\forall v_j \in V} | w_X(v_i,v_j) - w_Y(v_i,v_j) | \qquad (9)$$

It can detect the maximum difference between two brain networks. Figure 9 shows the bottleneck distance maps of subject-wise networks and group-wise networks among AD-MCI-NC. As we see in the figure, the latter difference is indeed more obvious. To validate the sensitivity to subtle changes in network structure, we directly conducted statistical hypothesis testing on all measures under subject-wise networks. In this condition, only our proposed SIP obtained a significant difference among all three groups of AD, MCI and NC at 0.01 level ($p = .002$) under L-AAL90 atlas, whereas few other comparative measures can obtain a significance level of 0.05 even for single between-group differences (Table 2). In addition, the subject-wise network improves the ease of statistic inference and computation efficiency. Most prior persistent homology-based research has conducted statistical inference under group-wise networks. Their computation costs are relatively high as all subjects in a

TABLE 3 Reproducibility of statistical analysis with different network measures over various parcellation schemes

	Measure					
Parcellation	SIP	BNP	CPL	ND	EC	Mod
Group difference between AD vs MCI						
L-HOA112	**0.044**[c]	0.280	0.433	0.202	0.245	0.475
L-AAL116	**0.024**[c]	0.458	0.352	0.367	0.228	0.464
L-Crad200	**0.043**[c]	0.344	0.147	0.444	0.048[c]	0.157
H-1024	**0.031**[c]	0.323	0.299	0.088[a]	0.098[b]	0.470
Group difference between AD vs NC						
L-HOA112	**0.007**[b]	0.046[c]	0.252	0.399	0.192	0.221
L-AAL116	**0.002**[b]	0.046[c]	0.238	0.213	0.096[a]	0.154
L-Crad200	**0.008**[b]	0.071[a]	0.460	0.194	0.030[c]	0.367
H-1024	**0.025**[c]	0.295	0.393	0.491	0.091[a]	0.181
Group difference between MCI vs NC						
L-HOA112	0.223	**0.122**	0.190	0.272	0.423	0.226
L-AAL116	0.196	**0.053**[a]	0.092 [a]	0.094[a]	0.373	0.156
L-Crad200	0.218	0.133	0.154	0.147	0.447	**0.077** [a]
H-1024	**0.047**[c]	0.462	0.207	0.077[a]	0.388	0.091 [a]
Group difference among AD vs MCI vs NC						
L-HOA112	**0.047**[c]	0.209	0.700	0.934	0.973	0.881
L-AAL116	**0.019**[c]	0.307	0.497	0.453	0.727	0.705
L-Crad200	**0.079**[a]	0.360	0.609	0.502	0.442	0.664
H-1024	**0.045**[c]	0.626	0.675	0.515	0.797	0.879

Threshold selection: The first two measures are threshold-free, while the last four measures take the significant network edges by Bonferroni correction method with corrected p value <.05.
Measures: SIP: the slope of IPF plot; BNP: the zeroth Betti numbers plot (Chung et al., 2015; Lee et al., 2012; Lee et al., 2017); CPL: characteristic path length (Brier et al., 2014; Wang et al., 2013); ND: network diameter (Assenov et al., 2007; Fagerholm et al., 2015); EC: eigenvector centrality (Binnewijzend et al., 2012; Qiu et al., 2016); Mod: modularity (Sporns & Betzel, 2016; Tagliazucchi et al., 2013).
Parcellations: L-HOA112, low-resolution Harvard-Oxford atlas with 112 ROIs (Kennedy et al., 1998; Makris et al., 1999); L-AAL116, low-resolution automated anatomical labeling atlas with 116 ROIs (Tzourio-Mazoyer et al., 2002); L-Crad200, low-resolution Craddock et al. functional atlas with 200 ROIs (Craddock et al., 2012); H-1024, randomly generated high-resolution atlas with 1,024 ROIs (Zalesky et al., 2010).
The p value was obtained using 10,000 permutation test between two single groups and Kruskal–Wallis test (Hollander et al., 1973) for multiple comparisons among all three groups by R software respectively (Team, 2014). The minimum p value in each row is bold.
[a] $.05 < p < .1$.
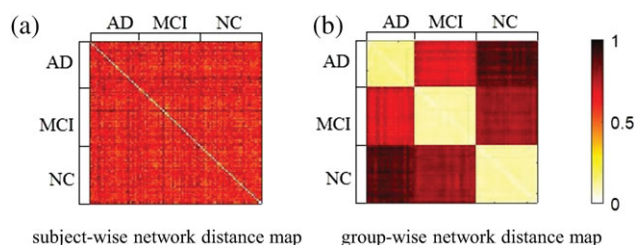[b] $p < .01$.
[c] $.01 \leq p \leq .05$.

FIGURE 9 Bottleneck distance maps of subject-wise networks (a) and group-wise networks (b). The group-wise networks were obtained by leave-one-out jackknife resampling method. In each map, the three diagonal block matrices with the size 31×31, 38×38, and 37×37 measure the distance between networks within a group and the off-diagonal block matrices measure the distance between groups [Color figure can be viewed at wileyonlinelibrary.com]

specific group have to be involved. For example, it was reported that the group difference analysis by permutation test with 10,000 permutations could not be implemented because it would take about 7 days of computation in their experimental environment (Chung et al., 2015). By constructing subject-wise multiscale RSN, our methods are less demanding for large cohort subject numbers and, as a result, gain about 31-time efficiency in the case of permutation test with ten-thousand permutations in our experiments.

4.2 | Threshold-free versus threshold-dependent

The edges in a weighted network usually reflect the measurement of correlation or coherence of activity between nodes. It is common to threshold an original network to obtain a sparser one according to the significance of connections (Binnewijzend et al., 2012; Smith & Nichols, 2009; Wang et al., 2013) or the desired sparsity (Eavani et al., 2015; Wee, Yang, Yap, Shen, & AsDN, 2016) before quantifying graph theoretical features. However, such a threshold-dependent scheme may discard a great deal of potential important information from original network and may cause ineffectiveness (Giusti et al., 2016). In addition, it is difficult to make a principled choice of such thresholds. In our threshold-free framework using graph filtration, we do not need to specify any parameters to obtain thresholding matrix because all possible thresholds are exactly the edge weights of MST and thus the multiscale subnetworks are constructed automatically. As this

framework retains most of the original network information in the resulting nested subnetworks, it may be more effective for brain network analysis.

To compare with the threshold-free measures (SIP and BNP), we adopted two thresholding schemes for the threshold-dependent measures (CPL, ND, EC, and Mod) and the thresholding weighed networks were then examined. First, a general practice for the choice of threshold is the multiple comparison correction over every possible edge (Wang et al., 2013). The original weighted network matrix elements whose corresponding p values passed through a statistical threshold are retained. The experimental results of threshold-dependent measures in Tables 2 and 3 were obtained when we selected network edges by Bonferroni correction method with corrected p value<.05. As these threshold-dependent measures could not detect significant difference under this scheme, we performed the second scheme that thresholds weighted network repeatedly over a wide range of sparsity (He, Chen, & Evans, 2008). We tried 80 sparsity thresholds by iteratively deleting 11%–90% of the edges with the largest weights (i.e., the weakest functional connectivity) from the original RSN over L-AAL90 atlas for threshold-dependent measures, and recorded the lowest p values of AD versus MCI versus NC from these thresholds in Table 4. It should be noticed that we have not applied such thresholding schemes on the threshold-free measurers as they run the omni-thresholding framework automatically. Even under such an unfair competitive condition, our threshold-free SIP does not lose as it may consist of comprehensive information after multiscale thresholding.

Although there are some similar existing multi-thresholding studies on brain network research (Achard, Salvador, Whitcher, Suckling, & Bullmore, 2006; He et al., 2008; Kim et al., 2015; Supekar et al., 2008) that have been used in modeling connectivity matrices at many different thresholds or scales, they usually only have limited generality because the determination of thresholding set is relatively arbitrary. Moreover, they are usually used to visualize how the feature varies over different thresholds but the pattern of change is rarely quantified. In contrast, persistent homology-based framework (Choi et al., 2014; Chung et al., 2015; Giusti et al., 2016; Lee et al., 2012; Lee et al., 2017; Yoo et al., 2017) can be used to quantify such dynamic patterns in a more general and coherent way.

TABLE 4 Most significant results of threshold-dependent measures by removing a certain percentage edges

Between-group	Threshold-free measure		Threshold-dependent measure			
	SIP	BNP	CPL (70%)	ND (20%)	EC (80%)	Mod (90%)
AD vs MCI	0.046	0.499	**0.001**	0.103	0.020	0.019
AD vs NC	**0.0006**	0.016	0.001	0.023	0.007	0.036
MCI vs NC	0.033	**0.011**	0.481	0.231	0.345	0.399
AD vs MCI vs NC	**0.002**	0.073	0.003	0.137	0.030	0.083

Threshold-free measure: The p values are copied from Table 2 for visual comparison.
Threshold-dependent measure: We tried 80 sparsity thresholds by iteratively deleting top 11%–90% edges of the weakest functional connectivity from original RSN. The four threshold-dependent measures detect the best p values of AD versus MCI versus NC if we remove top 70%, 20%, 80%, and 90% weakest functional connectivity, respectively.
Measures: SIP: the slope of IPF plot; BNP: the zeroth Betti numbers plot (Chung et al., 2015; Lee et al., 2012; Lee et al., 2017); CPL: characteristic path length (Brier et al., 2014; Wang et al., 2013); ND: network diameter (Assenov et al., 2007; Fagerholm et al., 2015); EC: eigenvector centrality (Binnewijzend et al., 2014; Qiu et al., 2016); Mod: modularity (Sporns & Betzel, 2016; Tagliazucchi et al., 2013).
The p value was obtained using 10,000 permutation test between two single groups and Kruskal–Wallis test (Hollander et al., 1973) for multiple comparisons among all three groups by R software (Team, 2014). The minimum p value in each row is bold.

Between-group	AUC of IPF plot	AUC of BNP
AD vs MCI	**0.027**	0.108
AD vs NC	**0.043**	0.154
MCI vs NC	0.416	**0.412**
AD vs MCI vs NC	**0.084**	0.641

The p value was obtained using 10,000 permutation test between two single groups and Kruskal–Wallis test (Hollander et al., 1973) for multiple comparisons among all three groups by R software (Team, 2014). The minimum p value in each row is bold. In general, the proposed IPF plot detects better significance than the compared BNP when the AUC-based method is applied.

4.3 | From multivariate statistics to a univariate measure

In the graph filtration of brain networks, there are a set of persistent statistics as every subgraph has a feature at each filtration value. To compare the networks between disease and health, some studies have summarized these multivariate features into univariate using AUC-based methods which estimate area under the curves of persistent feature plots over all filtration values (Chung et al., 2015; Giusti, Pastalkova, Curto, & Itskov, 2015). Others (Khalid, Kim, Chung, Ye, & Jeon, 2014; Lee et al., 2012) applied linear regression analysis to compute the slope of the BNP as it follows a monotonic function. In our study, we deliberately designed a monotonically decreasing convergence function so that we can quantify the proposed IPF by its slope. All the results of the proposed IPF plots and the comparison BNPs in Section 3.2 were obtained using the slope's approach. In addition, we also investigated the AUC-based method in our experiments and the obtained p values are shown in Table 5. In general, the proposed IPF plot detects better significance than the comparison BNP when the AUC-based method is applied. In addition, the experimental results are not better than those achieved by the slope-based method (Table 2) especially for BNP. As the proposed IPF plot and the comparison BNP are both monotonically decreasing convergence functions, the slope-based methods may better reflect the changes of persistent feature over all possible scales.

4.4 | MCI converters vesus nonconverters

Patients with MCI represent an important clinical group as they are at increased risk of MCI (Okello et al., 2009). It is a challenging problem to study the difference between MCI converters and non-converters. There are only 2 out of all 38 MCI patients converting to AD within 2 years in our current dataset. In order to further study the conversion of MCI patients to AD, we added all other 8 MCI converters from ADNI2 dataset during a 2-year follow-up period after their baseline rs-fMRI. We compared the difference of SIP between MCI converters ($n = 10$) and non-converters ($n = 36$) at the baseline, and found their difference are tend to be significant by 10,000 permutation tests (p value = .088). The absolute mean value of SIP of MCI converters is smaller than that of MCI nonconverters, and is closer to that of AD group. Although further rigorous studies which involve more subjects and longitudinal imaging data analysis, for example, Cox hazard model (Cox, 1972), is warranted for this line of research, our research results

may provide valuable insights for MCI conversion research by rs-fMRI analyses.

4.5 | Relationship of SIP to biological processes

Similar to the zeroth Betti number, the IPF is a persistent topology feature and its plot is a monotonically decreasing convergence function. It quantifies the topological changes of a network when the connected components are aggregating into a bigger one. In this way, the proposed network measure SIP can be thought as the information diffusion rate or convergence speed of arriving at a fully connected component. In this study, the computed group SIPs show a pattern, AD < MCI < NC, with the significance level $p = .002$ based on the Kruskal–Wallis test. The fact that SIP curves are less steepening with AD and MCI groups than with NC may imply a slower information diffusion rate in AD and MCI groups. Furthermore, the SIP is directly related to the whole-brain network topology, suggesting the contribution to the observed global topological abnormalities. Therefore, it is reasonable to speculate that the slow convergence speed is caused by decreased functional integration throughout the brain, which may further be responsible for cognitive deficits in patients. This finding is consistent with previous reports of the impaired global organization and disrupted neuronal integration in AD dementia and MCI patients (Blennow, De Leon, & Zetterberg, 2006; Sanz-Arigita et al., 2010; Sorg et al., 2007; Stam et al., 2006; Van Der Flier et al., 2002; Wang et al., 2013). In Figure 6, we found there are relatively dense short-distant (<0.25) connected components and relatively spare long-distance (≥0.25) connected components in MCI and AD groups comparing to NC group. Progress in clinical stages from MCI to AD may result in more disruptions of long-distant components, so it may be encouraged to establish short-distant components as alternative connections to keep information transmission between two distant regions. Overall, our results provide some empirical evidence for disrupted network organization in AD dementia and MCI patients at the global level.

4.6 | Potential future improvements

There are at least four main caveats when applying the proposed persistent feature. First, we only used the zeroth Betti number β_0 in this study but it is possible to integrate higher degree Betti numbers in our framework. The current IPF plot shows how the disconnected subcomponents are integrated into a fully connected component when the filtration value increases, but it does not consider how the subcomponents are densely or sparsely connected. The sparse network tends to have more holes and the Betti number β_1 has the potential to measure the number of holes in a network. The higher Betti numbers are usually identified using persistent homology-based kernel (Kusano, Hiraoka, & Fukumizu, 2016). In the specific case of the first Betti number, a study has reported that the hole in the metabolic network of AD can be detected based on persistent homology and 1-Laplacian (Lee, Chung, Kang, & Lee, 2014). To some extent, our proposed feature IPF is an integral of the persistence of the zeroth homology. If we also define the total persistence of the first homology in a similar way (Cohen-Steiner, Edelsbrunner, Harer, & Mileyko, 2010) and combine it with our current feature IPF, we may extend

our work to higher Betti numbers. Thus, we may quantify the integration of the whole brain regions and the sparsity of connected regions. Second, the longitudinal characteristics of RSN remain to be determined. In this study, we only investigated the brain network dynamics in cross sectional images. With longitudinal brain images, we may further study the evolution between longitudinal brain networks by quantifying the difference of their persistent features. Although there is no longitudinal study using persistent homology features, the existing integrated brain network research on BNP (Chung et al., 2017; Lee et al., 2017) may inspire some ideas for its future applications in AD research. Third, additional studies are needed to clarify the ability of the proposed SIP to detect and track AD, provide diagnostic or prognostic value, or assist in the evaluation of disease-slowing treatments. Here we did not categorize subjects based on amyloid, tau, or other neurodegenerative biomarker criteria because not all of the subjects had biomarker data available. The diagnostic classification of AD, MCI, and NC was made by ADNI investigators using some established criteria (McKhann et al., 1984; McKhann et al., 2011; Petersen et al., 2001). We checked these diagnostic classifications with amyloid biomarkers for 47 available subjects and found they concur with the diagnostic statuses. However, for more reliable results, in future work, we intend to enrich our dataset and further study the performance of our proposed network measure in discriminating groups of cognitively unimpaired amyloid negative versus cognitively unimpaired amyloid positive, MCI amyloid negative versus MCI amyloid positive and dementia amyloid negative versus dementia amyloid positive (Langbaum et al., 2013; Wu et al., 2018). Finally, our current results should be viewed as exploratory and need to be further confirmed in other independent cohorts in future (Tomše et al., 2017). Similar to some prior work (Khazaee et al., 2016) where the integration of single global network features with other local feature boosted fMRI network classification performance, our proposed univariate SIP may achieve satisfying classification performance when combining with other local features to take advantage some advanced machine learning methods like support vector machine (Cortes & Vapnik, 1995), and so forth. We further hypothesize that the adoption of some machine learning techniques, such as nonlinear kernel machine (Hofmann, Scholkopf, & Smola, 2008), may help improve its classification performance. Overall, this work presents our initial efforts to enrich persistent brain network analysis features. We hope our preliminary results could inspire new ideas and further advance persistent homology-based brain network analysis research.

5 | CONCLUSION

In this article, we present a novel network measure to complement the mathematical theory of BNP by integrating an additional feature of connected component aggregation cost with BNP to achieve holistic descriptions of graph evolutions and quantify brain network dynamics. We apply the new measure to study the RSN in AD research and release our software source code and experimental data to the public. Our method offers a novel insight into the whole-brain network analysis and the proposed measure SIP differentiates AD dementia and MCI patients from healthy individuals with improved performance compared to other widely used measures. The experimental results provide empirical evidence for disrupted network organization in AD dementia and MCI patients at a global level, and suggest that our SIP may be a potential imaging biomarker of AD. In the future, we will validate our method in other independent cohorts. We will also explore its broad applications for the preclinical AD research (Langbaum et al., 2013), such as building univariate Cox proportional hazard models to determine the hazard ratio for progression into AD (Chen et al., 2011) and reducing sample sizes for the AD clinical trials (Gutman, et al., 2013).

ORCID

Kewei Chen 🆔 https://orcid.org/0000-0001-8497-3069

Yalin Wang 🆔 https://orcid.org/0000-0002-6241-735X

REFERENCES

Achard, S., Salvador, R., Whitcher, B., Suckling, J., & Bullmore, E. (2006). A resilient, low-frequency, small-world human brain functional network with highly connected association cortical hubs. *The Journal of Neuroscience*, 26(1), 63–72. https://doi.org/10.1523/jneurosci.3874-05.2006

Adams H, Tausz A, Vejdemo-Johansson M. (2014). JavaPlex: A research software package for persistent (co) homology. In International Congress on Mathematical Software, Berlin, Heidelberg, pp. 129–136.

Ait-Aoudia, S., Jegou, R., & Michelucci, D. (2014). Reduction of constraint systems. *arXiv* 1405.6131.

Assenov, Y., Ramírez, F., Schelhorn, S.-E., Lengauer, T., & Albrecht, M. (2007). Computing topological parameters of biological networks. *Bioinformatics*, 24(2), 282–284.

Bai, F., Zhang, Z., Watson, D. R., Yu, H., Shi, Y., Yuan, Y., ... Qian, Y. (2009). Abnormal functional connectivity of hippocampus during episodic memory retrieval processing network in amnestic mild cognitive impairment. *Biological Psychiatry*, 65(11), 951–958.

Beckmann, C. F., DeLuca, M., Devlin, J. T., & Smith, S. M. (2005). Investigations into resting-state connectivity using independent component analysis. *Philosophical Transactions of the Royal Society of London B: Biological Sciences*, 360(1457), 1001–1013.

Bernhardt, B. C., Chen, Z., He, Y., Evans, A. C., & Bernasconi, N. (2011). Graph-theoretical analysis reveals disrupted small-world organization of cortical thickness correlation networks in temporal lobe epilepsy. *Cerebral Cortex*, 21(9), 2147–2157.

Binnewijzend, M. A., Adriaanse, S. M., Flier, W. M., Teunissen, C. E., Munck, J. C., Stam, C. J., ... Wink, A. M. (2014). Brain network alterations in Alzheimer's disease measured by eigenvector centrality in fMRI are related to cognition and CSF biomarkers. *Human Brain Mapping*, 35(5), 2383–2393.

Binnewijzend, M. A., Schoonheim, M. M., Sanz-Arigita, E., Wink, A. M., Van Der Flier, W. M., Tolboom, N., ... Van Berckel, B. N. (2012). Resting-state fMRI changes in Alzheimer's disease and mild cognitive impairment. *Neurobiology of Aging*, 33(9), 2018–2028.

Biswal, B., Zerrin Yetkin, F., Haughton, V. M., & Hyde, J. S. (1995). Functional connectivity in the motor cortex of resting human brain using echo-planar MRI. *Magnetic Resonance in Medicine*, 34(4), 537–541.

Biswal, B. B., Mennes, M., Zuo, X.-N., Gohel, S., Kelly, C., Smith, S. M., ... Colcombe, S. (2010). Toward discovery science of human brain function. *Proceedings of the National Academy of Sciences of the United States of America*, 107(10), 4734–4739.

Blennow, K., De Leon, M. J., & Zetterberg, H. (2006). Alzheimer's disease. *The Lancet*, 368(9533), 387–403. https://doi.org/10.1016/S0140-6736(06)69113-7

Braun, U., Muldoon, S. F., & Bassett, D. S. (2015). On human brain networks in health and disease. *eLS*, 22(4), 340–347.

Brier, M. R., Thomas, J. B., Fagan, A. M., Hassenstab, J., Holtzman, D. M., Benzinger, T. L., ... Ances, B. M. (2014). Functional connectivity and graph theory in preclinical Alzheimer's disease. *Neurobiology of Aging*, 35(4), 757–768.

Buldú, J. M., Bajo, R., Maestú, F., Castellanos, N., Leyva, I., Gil, P., ... Del-Pozo, F. (2011). Reorganization of functional networks in mild cognitive impairment. *PLoS One*, 6(5), e19584.

Bullmore, E., & Sporns, O. (2009). Complex brain networks: Graph theoretical analysis of structural and functional systems. *Nature Reviews Neuroscience*, 10(3), 186–198.

Carlsson, G., & Mémoli, F. (2008). Persistent clustering and a theorem of J. Kleinberg. *arXiv* 0808.2241.

Caroli, A., Prestia, A., Chen, K., Ayutyanont, N., Landau, S. M., Madison, C. M., ... Reiman, E. M. (2012). Summary metrics to assess Alzheimer disease–related hypometabolic pattern with 18F-FDG PET: Head-to-head comparison. *Journal of Nuclear Medicine*, 53(4), 592–600.

Chazal, F., Glisse, M., Labruere, C., & Michel, B. (2013). Optimal rates of convergence for persistence diagrams in topological data analysis. *arXiv* 1305.6239.

Chen C, Edelsbrunner H. (2011). Diffusion runs low on persistence fast. In IEEE International Conference on Computer Vision, Barcelona, Spain, pp. 423–430.

Chen, K., Ayutyanont, N., Langbaum, J. B., Fleisher, A. S., Reschke, C., Lee, W., ... Reiman, E. M. (2011). Characterizing Alzheimer's disease using a hypometabolic convergence index. *NeuroImage*, 56(1), 52–60. https://doi.org/10.1016/j.neuroimage.2011.01.049

Choi, H., Kim, Y. K., Kang, H., Lee, H., Im, H.-J., Kim, E. E., ... Lee, D. S. (2014). Abnormal metabolic connectivity in the pilocarpine-induced epilepsy rat model: A multiscale network analysis based on persistent homology. *NeuroImage*, 99, 226–236.

Chung, M. K., Hanson, J. L., Ye, J., Davidson, R. J., & Pollak, S. D. (2015). Persistent homology in sparse regression and its application to brain morphometry. *IEEE Transactions on Medical Imaging*, 34(9), 1928–1939.

Chung MK, Villalta-Gil V, Lee H, Rathouz PJ, Lahey BB, Zald DH. (2017). Exact topological inference for paired brain networks via persistent homology. In International Conference on Information Processing in Medical Imaging, Boone, NC, pp. 299–310.

Cohen, A. D., & Klunk, W. E. (2014). Early detection of Alzheimer's disease using PiB and FDG PET. *Neurobiology of Disease*, 72, 117–122.

Cohen-Steiner, D., Edelsbrunner, H., Harer, J., & Mileyko, Y. (2010). Lipschitz functions have L p-stable persistence. *Foundations of Computational Mathematics*, 10(2), 127–139.

Cordes, D., Haughton, V. M., Arfanakis, K., Carew, J. D., Turski, P. A., Moritz, C. H., ... Meyerand, M. E. (2001). Frequencies contributing to functional connectivity in the cerebral cortex in "resting-state" data. *American Journal of Neuroradiology*, 22(7), 1326–1333.

Cortes, C., & Vapnik, V. (1995). Support-vector networks. *Machine Learning*, 20(3), 273–297. https://doi.org/10.1023/a:1022627411411

Cox, D. R. (1972). Regression models and life-tables. *Journal of the Royal Statistical Society. Series B, Methodological*, 34(2), 187–220.

Craddock, R. C., James, G. A., Holtzheimer, P. E., Hu, X. P., & Mayberg, H. S. (2012). A whole brain fMRI atlas generated via spatially constrained spectral clustering. *Human Brain Mapping*, 33(8), 1914–1928.

Dai, Z., & He, Y. (2014). Disrupted structural and functional brain connectomes in mild cognitive impairment and Alzheimer's disease. *Neuroscience Bulletin*, 30(2), 217–232. https://doi.org/10.1007/s12264-013-1421-0

Dai, Z., Yan, C., Li, K., Wang, Z., Wang, J., Cao, M., ... He, Y. (2015). Identifying and mapping connectivity patterns of brain network hubs in Alzheimer's disease. *Cerebral Cortex*, 25(10), 3723–3742. https://doi.org/10.1093/cercor/bhu246

Damoiseaux, J. S., & Greicius, M. D. (2009). Greater than the sum of its parts: A review of studies combining structural connectivity and resting-state functional connectivity. *Brain Structure and Function*, 213(6), 525–533.

De Haan, W., Van Der Flier, W. M., Koene, T., Smits, L. L., Scheltens, P., & Stam, C. J. (2012). Disrupted modular brain dynamics reflect cognitive dysfunction in Alzheimer's disease. *NeuroImage*, 59(4), 3085–3093.

De Silva, V., & Ghrist, R. (2007). Homological sensor networks. *Notices of the American Mathematical Society*, 54(1), 10–17.

DeSalvo, M. N., Douw, L., Tanaka, N., Reinsberger, C., & Stufflebeam, S. M. (2013). Altered structural connectome in temporal lobe epilepsy. *Radiology*, 270(3), 842–848.

Dimitriadis, S. I., Laskaris, N. A., Tsirka, V., Vourkas, M., Micheloyannis, S., & Fotopoulos, S. (2010). Tracking brain dynamics via time-dependent network analysis. *Journal of Neuroscience Methods*, 193(1), 145–155. https://doi.org/10.1016/j.jneumeth.2010.08.027

Eavani, H., Satterthwaite, T. D., Filipovych, R., Gur, R. C., Gur, R. C., & Davatzikos, C. (2015). Identifying sparse connectivity patterns in the brain using resting-state fMRI. *NeuroImage*, 105, 286–299.

Edelsbrunner, H., & Harer, J. (2010). *Computational topology: An introduction*. Brooklyn, NY: American Mathematical Society.

Edelsbrunner H, Letscher D, Zomorodian A. (2000). Topological persistence and simplification. In Proceedings of the 41st annual symposium on foundations of computer science, Redondo Beach, CA, p. 454–463.

Fagerholm, E. D., Hellyer, P. J., Scott, G., Leech, R., & Sharp, D. J. (2015). Disconnection of network hubs and cognitive impairment after traumatic brain injury. *Brain*, 138(6), 1696–1709.

Folstein, M. F., Folstein, S. E., & McHugh, P. R. (1975). Mini-mental state: A practical method for grading the cognitive state of patients for the clinician. *Journal of Psychiatric Research*, 12(3), 189–198.

Fox, M. D., & Raichle, M. E. (2007). Spontaneous fluctuations in brain activity observed with functional magnetic resonance imaging. *Nature Reviews. Neuroscience*, 8(9), 700–711. https://doi.org/10.1038/nrn2201

Fox, M. D., Zhang, D., Snyder, A. Z., & Raichle, M. E. (2009). The global signal and observed anticorrelated resting state brain networks. *Journal of Neurophysiology*, 101(6), 3270–3283.

Freedman, D., & Chen, C. (2009). Computer Vision. Hauppauge, New York: Nova Science Pub. Inc.

Ghrist, R. (2008). Barcodes: The persistent topology of data. *Bulletin of the American Mathematical Society*, 45(1), 61–75.

Giusti, C., Ghrist, R., & Bassett, D. S. (2016). Two's company, three (or more) is a simplex : Algebraic-topological tools for understanding higher-order structure in neural data. *Journal of Computational Neuroscience*, 41(1), 1–14. https://doi.org/10.1007/s10827-016-0608-6

Giusti, C., Pastalkova, E., Curto, C., & Itskov, V. (2015). Clique topology reveals intrinsic geometric structure in neural correlations. *Proceedings of the National Academy of Sciences of the United States of America*, 112(44), 13455–13460. https://doi.org/10.1073/pnas.1506407112

Gower, J. C., & Ross, G. J. (1969). Minimum spanning trees and single linkage cluster analysis. *Applied Statistics*, 18, 54–64.

Gutman, B. A., Hua, X., Rajagopalan, P., Chou, Y. Y., Wang, Y., Yanovsky, I., ... Alzheimer's Disease Neuroimaging Initiative. (2013). Maximizing power to track Alzheimer's disease and MCI progression by LDA-based weighting of longitudinal ventricular surface features. *NeuroImage*, 70, 386–401. https://doi.org/10.1016/j.neuroimage.2012.12.052

Hage, P., & Harary, F. (1995). Eccentricity and centrality in networks. *Social Networks*, 17(1), 57–63.

Han, Y., Wang, J., Zhao, Z., Min, B., Lu, J., Li, K., ... Jia, J. (2011). Frequency-dependent changes in the amplitude of low-frequency fluctuations in amnestic mild cognitive impairment: A resting-state fMRI study. *NeuroImage*, 55(1), 287–295. https://doi.org/10.1016/j.neuroimage.2010.11.059

He, Y., Chen, Z., & Evans, A. (2008). Structural insights into aberrant topological patterns of large-scale cortical networks in Alzheimer's disease. *Journal of Neuroscience*, 28(18), 4756–4766.

He, Y., Chen, Z., Gong, G., & Evans, A. (2009). Neuronal networks in Alzheimer's disease. *The Neuroscientist*, 15(4), 333–350.

He, Y., & Evans, A. (2010). Graph theoretical modeling of brain connectivity. *Current Opinion in Neurology*, 23(4), 341–350.

Hofmann, T., Scholkopf, B., & Smola, A. J. (2008). Kernel methods in machine learning. *The Annals of Statistics*, 36(3), 1171–1220.

Hollander, M., Wolfe, D. A., & Chicken, E. (1973). *Nonparametric statistical methods*. New York, NY: Wiley.

Ito, K., Fukuyama, H., Senda, M., Ishii, K., Maeda, K., Yamamoto, Y., ... Fujiwara, K. (2015). Prediction of outcomes in mild cognitive impairment by using 18F-FDG-PET: A multicenter study. *Journal of Alzheimer's Disease*, 45(2), 543–552.

Jack, C. R., Petersen, R. C., Xu, Y., O'brien, P., Smith, G. E., Ivnik, R. J., ... Kokmen, E. (2000). Rates of hippocampal atrophy correlate with change in clinical status in aging and AD. *Neurology*, 55(4), 484–490.

Jack, C. R., Petersen, R. C., Xu, Y. C., O'Brien, P. C., Smith, G. E., Ivnik, R. J., ... Kokmen, E. (1999). Prediction of AD with MRI-based hippocampal volume in mild cognitive impairment. *Neurology*, 52(7), 1397–1397, 1403.

Jiang, L., & Zuo, X. N. (2016). Regional homogeneity: A multimodal, multiscale neuroimaging marker of the human connectome. *The Neuroscientist*, 22(5), 486–505. https://doi.org/10.1177/1073858415595004

Johnson, K. A., Minoshima, S., Bohnen, N. I., Donohoe, K. J., Foster, N. L., Herscovitch, P., ... Hartley, D. M. (2013). Appropriate use criteria for amyloid PET: A report of the amyloid imaging task force, the society of nuclear medicine and molecular imaging, and the Alzheimer's association. *Journal of Nuclear Medicine*, 54(3), 476–490.

Kennedy, D., Lange, N., Makris, N., Bates, J., Meyer, J., & Caviness, V., Jr. (1998). Gyri of the human neocortex: An MRI-based analysis of volume and variance. *Cerebral Cortex*, 8(4), 372–384.

Khalid, A., Kim, B. S., Chung, M. K., Ye, J. C., & Jeon, D. (2014). Tracing the evolution of multi-scale functional networks in a mouse model of depression using persistent brain network homology. *NeuroImage*, 101, 351–363. https://doi.org/10.1016/j.neuroimage.2014.07.040

Khazaee, A., Ebrahimzadeh, A., & Babajani-Feremi, A. (2016). Application of advanced machine learning methods on resting-state fMRI network for identification of mild cognitive impairment and Alzheimer's disease. *Brain Imaging and Behavior*, 10(3), 799–817. https://doi.org/10.1007/s11682-015-9448-7

Kim, W. H., Adluru, N., Chung, M. K., Okonkwo, O. C., Johnson, S. C., B Bendlin, B., & Singh, V. (2015). Multi-resolution statistical analysis of brain connectivity graphs in preclinical Alzheimer's disease. *NeuroImage*, 118, 103–117. https://doi.org/10.1016/j.neuroimage.2015.05.050

Kusano G, Hiraoka Y, Fukumizu K. (2016). Persistence weighted Gaussian kernel for topological data analysis. In International Conference on Machine Learning, New York, p. 2004–2013.

Landau, S. M., Mintun, M. A., Joshi, A. D., Koeppe, R. A., Petersen, R. C., Aisen, P. S., ... Jagust, W. J. (2012). Amyloid deposition, hypometabolism, and longitudinal cognitive decline. *Annals of Neurology*, 72(4), 578–586.

Langbaum, J. B., Fleisher, A. S., Chen, K., Ayutyanont, N., Lopera, F., Quiroz, Y. T., ... Reiman, E. M. (2013). Ushering in the study and treatment of preclinical Alzheimer disease. *Nature Reviews. Neurology*, 9(7), 371–381. https://doi.org/10.1038/nrneurol.2013.107

Lee H, Chung MK, Kang H, Lee DS. (2014). Hole Detection in Metabolic Connectivity of Alzheimer's Disease Using k−Laplacian. In International Conference on Medical Image Computing and Computer-Assisted Intervention, Boston, MA, USA, pp. 297–304.

Lee, H., Kang, H., Chung, M. K., Kim, B.-N., & Lee, D. S. (2012). Persistent brain network homology from the perspective of dendrogram. *IEEE Transactions on Medical Imaging*, 31(12), 2267–2277.

Lee, H., Kang, H., Chung, M. K., Lim, S., Kim, B. N., & Lee, D. S. (2017). Integrated multimodal network approach to PET and MRI based on multidimensional persistent homology. *Human Brain Mapping*, 38(3), 1387–1402.

Lee, M. H., Miller-Thomas, M. M., Benzinger, T. L., Marcus, D. S., Hacker, C. D., Leuthardt, E. C., & Shimony, J. S. (2016). Clinical resting-state fMRI in the preoperative setting: Are we ready for prime time? *Topics in Magnetic Resonance Imaging*, 25(1), 11–18.

Lee, M. H., Smyser, C. D., & Shimony, J. S. (2013). Resting-state fMRI: A review of methods and clinical applications. *American Journal of Neuroradiology*, 34(10), 1866–1872. https://doi.org/10.3174/ajnr.A3263

Li, S. J., Li, Z., Wu, G., Zhang, M. J., Franczak, M., & Antuono, P. G. (2002). Alzheimer disease: Evaluation of a functional MR imaging index as a marker. *Radiology*, 225(1), 253–259. https://doi.org/10.1148/radiol.2251011301

Liu, X., Wang, S., Zhang, X., Wang, Z., Tian, X., & He, Y. (2014). Abnormal amplitude of low-frequency fluctuations of intrinsic brain activity in Alzheimer's disease. *Journal of Alzheimer's Disease*, 40(2), 387–397. https://doi.org/10.3233/jad-131322

Liu, Y., Wang, K., Yu, C., He, Y., Zhou, Y., Liang, M., ... Jiang, T. (2008). Regional homogeneity, functional connectivity and imaging markers of Alzheimer's disease: A review of resting-state fMRI studies. *Neuropsychologia*, 46(6), 1648–1656. https://doi.org/10.1016/j.neuropsychologia.2008.01.027

Lo, C.-Y., Wang, P.-N., Chou, K.-H., Wang, J., He, Y., & Lin, C.-P. (2010). Diffusion tensor tractography reveals abnormal topological organization in structural cortical networks in Alzheimer's disease. *Journal of Neuroscience*, 30(50), 16876–16885.

Lynall, M.-E., Bassett, D. S., Kerwin, R., McKenna, P. J., Kitzbichler, M., Muller, U., & Bullmore, E. (2010). Functional connectivity and brain networks in schizophrenia. *Journal of Neuroscience*, 30(28), 9477–9487.

Makedonov, I., Chen, J. J., Masellis, M., & MacIntosh, B. J. (2016). Physiological fluctuations in white matter are increased in Alzheimer's disease and correlate with neuroimaging and cognitive biomarkers. *Neurobiology of Aging*, 37, 12–18. https://doi.org/10.1016/j.neurobiolaging.2015.09.010

Makris, N., Meyer, J. W., Bates, J. F., Yeterian, E. H., Kennedy, D. N., & Caviness, V. S. (1999). MRI-based topographic parcellation of human cerebral white matter and nuclei: II. Rationale and applications with systematics of cerebral connectivity. *NeuroImage*, 9(1), 18–45.

Malinen, S., Vartiainen, N., Hlushchuk, Y., Koskinen, M., Ramkumar, P., Forss, N., ... Hari, R. (2010). Aberrant temporal and spatial brain activity during rest in patients with chronic pain. *Proceedings of the National Academy of Sciences of the United States of America*, 107(14), 6493–6497.

Maria C, Boissonnat J-D, Glisse M, Yvinec M. (2014). The Gudhi library: Simplicial complexes and persistent homology. In International Congress on Mathematical Software, Seoul, South Korea, p. 167–174.

McKhann, G., Drachman, D., Folstein, M., Katzman, R., Price, D., & Stadlan, E. M. (1984). Clinical diagnosis of Alzheimer's disease report of the NINCDS-ADRDA work group under the auspices of department of health and human services task force on Alzheimer's disease. *Neurology*, 34(7), 939–939, 944.

McKhann, G. M., Knopman, D. S., Chertkow, H., Hyman, B. T., Jack, C. R., Kawas, C. H., ... Mayeux, R. (2011). The diagnosis of dementia due to Alzheimer's disease: Recommendations from the National Institute on Aging-Alzheimer's Association workgroups on diagnostic guidelines for Alzheimer's disease. *Alzheimer's & Dementia*, 7(3), 263–269.

Morris, J. C. (1993). The clinical dementia rating (CDR): Current version and scoring rules. *Neurology*, 43, 2412–2414.

Murphy, K., Birn, R. M., Handwerker, D. A., Jones, T. B., & Bandettini, P. A. (2009). The impact of global signal regression on resting state correlations: Are anti-correlated networks introduced? *NeuroImage*, 44(3), 893–905.

Murtagh, F. (1983). A survey of recent advances in hierarchical clustering algorithms. *The Computer Journal*, 26(4), 354–359.

Newman, M. E., & Girvan, M. (2004). Finding and evaluating community structure in networks. *Physical Review E*, 69(2), 026113.

Okello, A., Koivunen, J., Edison, P., Archer, H., Turkheimer, F., Någren, K., ... Fox, N. (2009). Conversion of amyloid positive and negative MCI to AD over 3 years: An 11C-PIB PET study. *Neurology*, 73(10), 754–760.

Petersen, R. C., Stevens, J. C., Ganguli, M., Tangalos, E. G., Cummings, J., & DeKosky, S. (2001). Practice parameter: Early detection of dementia: Mild cognitive impairment (an evidence-based review). Report of the quality standards Subcommittee of the American Academy of neurology. *Neurology*, 56(9), 1133–1142.

Petri, G., Expert, P., Turkheimer, F., Carhart-Harris, R., Nutt, D., Hellyer, P. J., & Vaccarino, F. (2014). Homological scaffolds of brain functional networks. *Journal of the Royal Society Interface*, 11(101), 20140873.

Poldrack, R. A. (2007). Region of interest analysis for fMRI. *Social Cognitive and Affective Neuroscience*, 2(1), 67–70.

Pothen, A., & Fan, C.-J. (1990). Computing the block triangular form of a sparse matrix. *ACM Transactions on Mathematical Software (TOMS)*, 16(4), 303–324.

Power, J. D., Barnes, K. A., Snyder, A. Z., Schlaggar, B. L., & Petersen, S. E. (2012). Spurious but systematic correlations in functional connectivity MRI networks arise from subject motion. *NeuroImage*, 59(3), 2142–2154.

Qiu, T., Luo, X., Shen, Z., Huang, P., Xu, X., Zhou, J., & Zhang, M. (2016). Disrupted brain network in progressive mild cognitive impairment measured by eigenvector centrality mapping is linked to cognition and cerebrospinal fluid biomarkers. *Journal of Alzheimers Disease*, 54(4), 1483–1493. https://doi.org/10.3233/JAD-160403

Rubinov, M., & Sporns, O. (2010). Complex network measures of brain connectivity: Uses and interpretations. *NeuroImage*, 52(3), 1059–1069.

Santarnecchi, E., Galli, G., Polizzotto, N. R., Rossi, A., & Rossi, S. (2014). Efficiency of weak brain connections support general cognitive functioning. *Human Brain Mapping*, 35(9), 4566–4582. https://doi.org/10.1002/hbm.22495

Sanz-Arigita, E. J., Schoonheim, M. M., Damoiseaux, J. S., Rombouts, S. A., Maris, E., Barkhof, F., ... Stam, C. J. (2010). Loss of 'small-world' networks in Alzheimer's disease: Graph analysis of FMRI resting-state functional connectivity. *PLoS One*, 5(11), e13788.

Satterthwaite, T. D., Elliott, M. A., Gerraty, R. T., Ruparel, K., Loughead, J., Calkins, M. E., ... Gur, R. E. (2013). An improved framework for confound regression and filtering for control of motion artifact in the preprocessing of resting-state functional connectivity data. *NeuroImage*, 64, 240–256.

Sheline, Y. I., & Raichle, M. E. (2013). Resting state functional connectivity in preclinical Alzheimer's disease. *Biological Psychiatry*, 74(5), 340–347. https://doi.org/10.1016/j.biopsych.2012.11.028

Smith, S. M., & Nichols, T. E. (2009). Threshold-free cluster enhancement: Addressing problems of smoothing, threshold dependence and localisation in cluster inference. *NeuroImage*, 44(1), 83–98. https://doi.org/10.1016/j.neuroimage.2008.03.061

Song, X.-W., Dong, Z.-Y., Long, X.-Y., Li, S.-F., Zuo, X.-N., Zhu, C.-Z., ... Zang, Y.-F. (2011). REST: A toolkit for resting-state functional magnetic resonance imaging data processing. *PLoS One*, 6(9), e25031.

Sorg, C., Riedl, V., Mühlau, M., Calhoun, V. D., Eichele, T., Läer, L., ... Zimmer, C. (2007). Selective changes of resting-state networks in individuals at risk for Alzheimer's disease. *Proceedings of the National Academy of Sciences of the United States of America*, 104(47), 18760–18765.

Sporns, O. (2011). The human connectome: A complex network. *Annals of the New York Academy of Sciences*, 1224(1), 109–125.

Sporns, O., & Betzel, R. F. (2016). Modular brain networks. *Annual Review of Psychology*, 67, 613–640.

Stam, C., Jones, B., Nolte, G., Breakspear, M., & Scheltens, P. (2006). Small-world networks and functional connectivity in Alzheimer's disease. *Cerebral Cortex*, 17(1), 92–99.

Stam, C. J., Tewarie, P., Van Dellen, E., van Straaten, E. C., Hillebrand, A., & Van Mieghem, P. (2014). The trees and the forest: Characterization of complex brain networks with minimum spanning trees. *International Journal of Psychophysiology*, 92(3), 129–138. https://doi.org/10.1016/j.ijpsycho.2014.04.001

Suk, H. I., Wee, C. Y., Lee, S. W., & Shen, D. (2016). State-space model with deep learning for functional dynamics estimation in resting-state fMRI. *NeuroImage*, 129, 292–307. https://doi.org/10.1016/j.neuroimage.2016.01.005

Supekar, K., Menon, V., Rubin, D., Musen, M., & Greicius, M. D. (2008). Network analysis of intrinsic functional brain connectivity in Alzheimer's disease. *PLoS Computational Biology*, 4(6), e1000100.

Tagliazucchi, E., Von Wegner, F., Morzelewski, A., Brodbeck, V., Borisov, S., Jahnke, K., & Laufs, H. (2013). Large-scale brain functional modularity is reflected in slow electroencephalographic rhythms across the human non-rapid eye movement sleep cycle. *NeuroImage*, 70, 327–339.

Teipel, S., Drzezga, A., Grothe, M. J., Barthel, H., Chételat, G., Schuff, N., ... Hoffmann, W. (2015). Multimodal imaging in Alzheimer's disease: Validity and usefulness for early detection. *The Lancet Neurology*, 14(10), 1037–1053.

Tewarie, P., van Dellen, E., Hillebrand, A., & Stam, C. J. (2015). The minimum spanning tree: An unbiased method for brain network analysis. *NeuroImage*, 104, 177–188. https://doi.org/10.1016/j.neuroimage.2014.10.015

Tomše, P., Jensterle, L., Grmek, M., Zaletel, K., Pirtošek, Z., Dhawan, V., ... Trošt, M. (2017). Abnormal metabolic brain network associated with Parkinson's disease: Replication on a new European sample. *Neuroradiology*, 59(5), 507–515.

Tong, T., Aganj, I., Ge, T., Polimeni, J. R., & Fischl, B. (2017). Functional density and edge maps: Characterizing functional architecture in individuals and improving cross-subject registration. *NeuroImage*, 158, 346–355.

Tsao, S., Gajawelli, N., Zhou, J., Shi, J., Ye, J., Wang, Y., & Leporé, N. (2017). Feature selective temporal prediction of Alzheimer's disease progression using hippocampus surface morphometry. *Brain and Behavior: A Cognitive Neuroscience Perspective*, 7(7), e00733.

Tzourio-Mazoyer, N., Landeau, B., Papathanassiou, D., Crivello, F., Etard, O., Delcroix, N., ... Joliot, M. (2002). Automated anatomical labeling of activations in SPM using a macroscopic anatomical parcellation of the MNI MRI single-subject brain. *NeuroImage*, 15(1), 273–289.

Van Dellen, E., Douw, L., Hillebrand, A., de Witt Hamer, P. C., Baayen, J. C., Heimans, J. J., ... Stam, C. J. (2014). Epilepsy surgery outcome and functional network alterations in longitudinal MEG: A minimum spanning tree analysis. *NeuroImage*, 86, 354–363. https://doi.org/10.1016/j.neuroimage.2013.10.010

Van Dellen, E., Sommer, I. E., Bohlken, M. M., Tewarie, P., Draaisma, L., Zalesky, A., ... Stam, C. J. (2018). Minimum spanning tree analysis of

the human connectome. *Human Brain Mapping*, *39*(6), 2455–2471. https://doi.org/10.1002/hbm.24014

Van Der Flier, W., Van Den Heuvel, D., Weverling-Rijnsburger, A., Spilt, A., Bollen, E., Westendorp, R., ... Van Buchem, M. (2002). Cognitive decline in AD and mild cognitive impairment is associated with global brain damage. *Neurology*, *59*(6), 874–879.

Van Dijk, K. R., Hedden, T., Venkataraman, A., Evans, K. C., Lazar, S. W., & Buckner, R. L. (2010). Intrinsic functional connectivity as a tool for human connectomics: Theory, properties, and optimization. *Journal of Neurophysiology*, *103*(1), 297–321.

Van Dijk, K. R., Sabuncu, M. R., & Buckner, R. L. (2012). The influence of head motion on intrinsic functional connectivity MRI. *NeuroImage*, *59*(1), 431–438.

Van Duinkerken, E., Schoonheim, M. M., IJzerman, R. G., Moll, A. C., Landeira-Fernandez, J., Klein, M., ... Wink, A. M. (2017). Altered eigenvector centrality is related to local resting-state network functional connectivity in patients with longstanding type 1 diabetes mellitus. *Human Brain Mapping*, *38*(7), 3623–3636.

Vlooswijk, M., Vaessen, M., Jansen, J., De Krom, M., Majoie, H., Hofman, P., ... Backes, W. (2011). Loss of network efficiency associated with cognitive decline in chronic epilepsy. *Neurology*, *77*(10), 938–944.

Wang, J., Wang, L., Zang, Y., Yang, H., Tang, H., Gong, Q., ... He, Y. (2009). Parcellation-dependent small-world brain functional networks: A resting-state fMRI study. *Human Brain Mapping*, *30*(5), 1511–1523.

Wang, J., Zuo, X., Dai, Z., Xia, M., Zhao, Z., Zhao, X., ... He, Y. (2013). Disrupted functional brain connectome in individuals at risk for Alzheimer's disease. *Biological Psychiatry*, *73*(5), 472–481. https://doi.org/10.1016/j.biopsych.2012.03.026

Wang, J., Zuo, X., & He, Y. (2010). Graph-based network analysis of resting-state functional MRI. *Frontiers in Systems Neuroscience*, *4*, 16. https://doi.org/10.3389/fnsys.2010.00016

Wang Y, Song Y, Rajagopalan P, An T, Liu K, Chou Y-Y, Gutman B, Toga AW, Thompson PM. (2011). Surface-based TBM boosts power to detect disease effects on the brain: An N=804 ADNI study. *NeuroImage 56*(4), 1993–2010. doi: https://doi.org/10.1016/j.neuroimage.2011.03.040

Watts, D. J., & Strogatz, S. H. (1998). Collective dynamics of 'small-world' networks. *Nature*, *393*(6684), 440–442.

Wee, C.-Y., Yang, S., Yap, P.-T., Shen, D., & AsDN, I. (2016). Sparse temporally dynamic resting-state functional connectivity networks for early MCI identification. *Brain Imaging and Behavior*, *10*(2), 342–356.

Weissenbacher, A., Kasess, C., Gerstl, F., Lanzenberger, R., Moser, E., & Windischberger, C. (2009). Correlations and anticorrelations in resting-state functional connectivity MRI: A quantitative comparison of preprocessing strategies. *NeuroImage*, *47*(4), 1408–1416.

Woo, C.-W., Krishnan, A., & Wager, T. D. (2014). Cluster-extent based thresholding in fMRI analyses: Pitfalls and recommendations. *NeuroImage*, *91*, 412–419.

Wu J, Zhang J, Shi J, Chen K, Caselli R, Reiman E, Wang Y. (2018). Hippocampus Morphometry Study on Pathology-Confirmed Alzheimer's Disease Patients with Surface Multivariate Mrophometry Statistics. In *IEEE International Symposium on BIOMEDICAL IMAGING: From Nano to Macro (ISBI)*, Washington, D.C.

Wu P, Chen C, Wang Y, Zhang S, Yuan C, Qian Z, Metaxas D, Axel L. (2017). Optimal topological cycles and their application in cardiac trabeculae restoration. In *International Conference on Information Processing in Medical Imaging*, Boone, NC, pp. 80–92.

Xi, Q., Zhao, X. H., Wang, P. J., Guo, Q. H., Yan, C. G., & He, Y. (2012). Functional MRI study of mild Alzheimer's disease using amplitude of low frequency fluctuation analysis. *Chinese Medical Journal*, *125*(5), 858–862.

Yan, C., & Zang, Y. (2010). DPARSF: A MATLAB toolbox for "pipeline" data analysis of resting-state fMRI. *Frontiers in Systems Neuroscience*, *4*, 13.

Yao, Z., Zhang, Y., Lin, L., Zhou, Y., Xu, C., & Jiang, T. (2010). Abnormal cortical networks in mild cognitive impairment and Alzheimer's disease. *PLoS Computational Biology*, *6*(11), e1001006. https://doi.org/10.1371/journal.pcbi.1001006

Yoo, K., Lee, P., Chung, M. K., Sohn, W. S., Chung, S. J., Na, D. L., ... Jeong, Y. (2017). Degree-based statistic and center persistency for brain connectivity analysis. *Human Brain Mapping*, *38*(1), 165–181.

Zalesky, A., Cocchi, L., Fornito, A., Murray, M. M., & Bullmore, E. (2012). Connectivity differences in brain networks. *NeuroImage*, *60*(2), 1055–1062.

Zalesky, A., Fornito, A., Harding, I. H., Cocchi, L., Yucel, M., Pantelis, C., & Bullmore, E. T. (2010). Whole-brain anatomical networks: Does the choice of nodes matter? *NeuroImage*, *50*(3), 970–983. https://doi.org/10.1016/j.neuroimage.2009.12.027

Zang, Y., Jiang, T., Lu, Y., He, Y., & Tian, L. (2004). Regional homogeneity approach to fMRI data analysis. *NeuroImage*, *22*(1), 394–400. https://doi.org/10.1016/j.neuroimage.2003.12.030

APPENDIX A: GRAPH FILTRATION

Given a weighted graph $X = (V, W)$ with a node set $V = \{1, 2, ... n\}$ and edge weights $W = (w_{ij})$, where w_{ij} is the weight between node i and j, we introduce a binary network $\mathcal{B}(X,\lambda)$ at a fixed threshold λ as a simplicial complex (Edelsbrunner, Letscher, & Zomorodian, 2000). The adjacency matrix $C = (c_{ij})$ of *binary network* $\mathcal{B}(X,\lambda)$ is defined as.

$$c_{ij}(X,\lambda) = \begin{cases} 1 & \text{if } w_{ij} \leq \lambda; \\ 0 & \text{otherwise}. \end{cases} \tag{A1}$$

Any edge weight lager than λ is excluded, otherwise it is retained and set to 1, thus a binary network $\mathcal{B}(X,\lambda)$ is constructed from the weighted graph X. When the threshold λ is changed, we construct a sequence of binary networks

$$\mathcal{B}(X,\lambda_0), \mathcal{B}(X,\lambda_1), \mathcal{B}(X,\lambda_2), \cdots$$

Each of the binary networks is a simplicial complex with 0-simplices (nodes) and 1-simplices (edges), and is a special case of the Rips complex (Ghrist, 2008). When the threshold λ increases, the subsequent Rips complex becomes larger than the entire previous Rips complex. The nested sequence of the Rips complexes is called *Rips filtration*, which is the main theme of persistent homology (Edelsbrunner & Harer, 2010; Freedman & Chen, 2009). Therefore, we can construct the filtration on the collection of binary networks.

$$\mathcal{B}(X,\lambda_0) \subset \mathcal{B}(X,\lambda_1) \subset \cdots \mathcal{B}(X,\lambda_m), \tag{A2}$$

for $0 = \lambda_0 < \lambda_1 < \cdots < \lambda_m$ and $\lambda_1, \lambda_2, \cdots, \lambda_m \in W$, which is a special case of Rips filtration, that is, *graph filtration*.

Figure 1 illustrates an example of graph filtration with 4 nodes. The left is an original weighted graph $X = (V, W)$ followed by 4 nested binary networks $\mathcal{B}(X,0) \subset \mathcal{B}(X,0.1) \subset \mathcal{B}(X,0.2) \subset \mathcal{B}(X,0.4)$ at 4 increasing filtration values 0, 0.1, 0.2, and 0.4, respectively. The topological features of the binary network will be changed according to the increase of filtration value λ (Ghrist, 2008). In Figure 1, we may also obtain another nested filtration graph, such as $\mathcal{B}(X,0) \subset \mathcal{B}(X,0.2) \subset \mathcal{B}(X,0.6)$ among many other possibilities. So how can we obtain a

unique filtration that can be used in characterizing graphs? The following method helps establish its uniqueness.

Given a weighted graph $X = (V, W)$ with m unique positive edge weights, if we sort the m unique positive edge weights $\lambda_1 < \cdots < \lambda_m$ in an ascending order, the maximal graph filtration is $\mathcal{B}(X,0) \subset \mathcal{B}(X,\lambda_1) \subset \cdots \subset \mathcal{B}(X,\lambda_m)$ according to Equation (A2). Further, the maximum level of its graph filtration is $m + 1$, and the form is unique (see Theorem 2 in (Chung et al., 2015)). The finiteness and uniqueness of the filtration levels over finite graphs have been already applied in some software packages such as JavaPlex (Adams et al., 2014) and Gudhi (Maria, Boissonnat, Glisse, & Yvinec, 2014). It should be noticed that a set of unique positive weights can be obtained by removing any multiplicative weights when identical edge weights exist.

APPENDIX B: BETTI NUMBERS

In a simplicial complex, a path between two nodes is a sequence of nodes such that from each of these nodes, there is an edge to the next node in the sequence. Two nodes are connected if there is at least one path between them. A *connected component* in the simplicial complex is a subset of nodes any two of which are connected. Betti numbers (Edelsbrunner et al., 2000) are used to distinguish topological spaces based on the connectivity of k-dimensional simplicial complex. The kth Betti number is the rank of the kth homology group, which counts the number of distinct k-dimensional holes or k-cycles. Specifically, the zeroth Betti number, β_0, refers to the number of connected components, and the first Betti number, β_1, is the number of one-dimensional or circular holes.

Generally, the maximal graph filtration can be quantified by plotting the change of Betti numbers and computed by using either single linkage dendrogram (SLD) (Lee et al., 2012), the Dulmage–Mendelsohn decomposition (Ait-Aoudia, Jegou, & Michelucci, 2014; Pothen & Fan, 1990), or existing simplicial complex approaches (Carlsson & Mémoli, 2008; De Silva & Ghrist, 2007; Edelsbrunner et al., 2000). In this study, we compute the zeroth Betti number β_0 by constructing SLD which is equivalent to building the MST (Lee et al., 2012). The detailed procedure is described in Section 2.2.2. In the case of a tree which is a special graph without cycle, we can conclude a much stronger statement than general graph as following.

Given $\lambda_0 = 0$, as well as a tree T with $m \geq 2$ nodes and unique positive edge weights $\lambda_1 < \lambda_2 < \cdots < \lambda_{m-1}$, the *zeroth Betti number* β_0 corresponding to the maximal graph filtration is defined as (Chung et al., 2015)

$$\beta_0(T,\lambda_i) = m-i, \ \ 0 \leq i \leq m-1 \quad (B1)$$

Therefore, a weighted graph filtration in Equation (A2) can be converted to a sequence of nested binary trees $\mathcal{B}(T,\lambda_0) \subset \mathcal{B}(T,\lambda_1) \subset \cdots \mathcal{B}(T,\lambda_m)$ by SLD if we only focus on the zeroth Betti number.

APPENDIX C: MONOTONICITY OF THE IPF PLOT

Proposition 1: Given $\lambda_0 = 0$, as well as a tree T with $m \geq 2$ nodes and unique positive edge weights $\lambda_1 < \lambda_2 < \cdots < \lambda_{m-1}$, the IPF plot corresponding to the maximal graph filtration determined by each edge weight, λ, is a monotonically decreasing convergence function.

Proof: As there are totally $m - 1$ edges in a tree T with m nodes, the maximum level of its graph filtration is m, and the maximal unique graph filtration is

$$\mathcal{B}(T,\lambda_0 = 0) \subset \mathcal{B}(T,\lambda_1) \subset \cdots \mathcal{B}(T,\lambda_{m-1}).$$

Let $\gamma(T,\lambda_i) = \frac{1}{m(m-1)}\beta_0(T,\lambda_i) \times l(T,\lambda_i)$, where $\beta_0(T, \lambda_i)$ and $l(T, \lambda_i)$ are the zeroth Betti number and connected component aggregation cost corresponding to the maximal graph filtration, respectively.

The zeroth Betti number $\beta_0(T, \lambda_i)$ corresponding to the maximal graph filtration is given by the coordinates

$$(\lambda_0,m),(\lambda_1,m-1),(\lambda_2,m-2),\cdots,(\lambda_{m-2},2),(\lambda_{m-1},1).$$

Obviously, the sequence of the zeroth Betti numbers is bounded and is decreased while filtration value changing from λ_0 to λ_{m-1}, thus $\beta_0(T, \lambda_i)$ is a monotonically decreasing convergence function.

Further, the connected component aggregation cost $l(T, \lambda_i)$ corresponding to the maximal graph filtration is given by the coordinates

$$\left(\lambda_0,\sum_{k=1}^{m-1}\lambda_k\right),\left(\lambda_1,\sum_{k=2}^{m-1}\lambda_k\right),\left(\lambda_2,\sum_{k=3}^{m-1}\lambda_k\right),\cdots,\left(\lambda_{m-2},\sum_{k=m-1}^{m-1}\lambda_k\right),(\lambda_{m-1},0).$$

As all edge weights are positive, the sequence of connected component aggregation cost is bounded and is decreased while filtration value changing from λ_0 to λ_{m-1}, thus $l(T, \lambda_i)$ is also a monotonically decreasing convergence function.

Because both $\beta_0(T, \lambda_i)$ and $l(T, \lambda_i)$ are non-negative and are monotonically decreasing convergence functions, $\gamma(T,\lambda_i) = \frac{1}{m(m-1)}\beta_0(T,\lambda_i)*l(T,\lambda_i)$ is also a monotonically decreasing convergence function.